Ultra-Fast Lattice Dynamics in Laser Excited Ferroelectric Thin Films

Diplomarbeit

vorgelegt der Fakultät für Physik

der Universität Duisburg-Essen

von

Michael Dominic Vattilana

Mai 2011

1. Gutachter: Prof. Dr. Uwe Bovensiepen

2. Gutachter: Prof. Dr. Marika Schleberger

Hiermit versichere ich, dass ich die vorliegende Arbeit selbständig ohne unzulässige Hilfe Dritter und nur unter Verwendung der angegebenen Hilfsmittel angefertigt habe.

Essen, 6. Mai 2011

Michael Dominic Vattilana

Abstract

We used femtosecond time-resolved x-ray diffraction methods to investigate the dynamic structural evolution of ferroelectric switching after optical excitation in thin $PbTiO_3$ and $Pb(Zr_{0.2}Ti_{0.8})O_3$ films. The Experiments were performed using fs short hard x-ray pulses in an pump-probe experimental setup at the LCLS Free Electron Laser in Stanford and the laser-plasma-based source at the Universität Duisburg-Essen. Due to the strong coupling between polarization, strain and electronic degree of freedom we observe the polarization state of the material by directly visualizing the atomic-scale dynamics.

Furthermore important improvements on the experimental setup were performed to enable more flexibility to a wider range of different samples.

Zusammenfassung

Wir verwenden hier Methoden femtosekunden Zeit-aufgelöster Röntgenbeugung um die dynamische strukturelle Entwicklung ferroelektrischen Schaltens nach optischer Anregung in dünnen $PbTiO_3$ und $Pb(Zr_{0.2}Ti_{0.8})O_3$ Filmen zu untersuchen. Diese Experimente wurden mit Hilfe harter fs Röntgenpulse in einem Pump-Probe Experiment am Freien Elektronen Laser LCLS in Stanford und an der Laser-Plasma-basierten Quelle an der Universität Duisburg-Essen durchgeführt. Aufgrund der starken Kopplung zwischen Polarization, Strain und elektronischen Freiheitsgraden, beobachten wir den Polarizationszustand des Materials direkt durch dynamische Prozesse auf atomarer Größenskala.

Ausserdem wurden wichtige Verbesserungen am experimentellen Aufbau durchgeführt um mehr Flexibilität für ein breiteres Spektrum an Experimenten zu schaffen.

Contents

Chapter 1

Introduction

The aim of this work is to study the transient ultra-fast lattice dynamics of ferroelectric thin film systems. Its mainly motivated by the question wether ultra-short intense laser pulses can be used to switch these material. This is important for future technological applications of these materials as well as for a fundamental understanding of how these complex systems work and my be controlled.

Ultra-fast time-resolved X-ray diffraction provides the unique opportunity to directly study the atomic motion in these materials associated with light-induced changes of the ferroelectric polarization on the relevant time-scale, that is femto- (10^{-15} s) to picoseconds (10^{-12}s).

This thesis is structured as follows:

Chapter 2 provides the basic principles needed to understand how the exciting technique of time-resolved X-ray diffraction (TRXD) works. It also deals with the effects observed in laser excited materials. An important section is the one about the rocking curves - due to the fact that this is what is observed in using these experimental techniques. We will see that a tremendous amount of information can be extracted by their observation. At the end of Chapter 2 the main properties of ferroelectric materials will be presented.

Chapter 3 presents the two fundamentally different X-ray sources used in the frame of this work - a laser-plasma-based source and a X-ray Free Electron Laser - and their experimental setups will be introduced in detail. A special part of this chapter is Section 3.3: Major improvements concerning the TRXD-setup at the Universität Duisburg-Essen will be presented in detail. This was a significant part of this diploma-thesis.

Chapter 4 will present and discuss tests regarding the improvements of the setup discussed in Chapter 3 with particular emphasis to perform time-resolved diffraction experiments on ferroelectric thin films.. Furthermore first results ofin experiments on ferroelectric thin films performed at the worlds only X-ray free electron laser, the LCLS in Stanford, are discussed.

Chapter 2

Basic Principles

This chapter will explain the basic principles of the experimental techniques used to investigate transient lattice dynamics by time-resolved X-ray diffraction. Therefore it is necessary to discuss the diffraction of light from crystal planes and how this can be done time-resolved. The second part of this chapter will then give an introduction to ferroelectric phenomena regarding the discussed experiments in Chapter 4.

2.1 Time-Resolved X-Ray Diffraction

Electromagnetic waves and waves of matter that interact with the atoms of a crystal are diffracted from the crystal lattice if their wavelength is of the same order of magnitude as the lattice parameter.For electromagnetic waves this is given for x-rays which have typical wavelengths of a few Angstroms (1 Å$= 10^{-10}$ m). X-rays are scattered by the electron shell of the lattice atoms and by constructive and destructive interference of the scattered waves typical diffraction patterns are formed.

From these diffraction patterns one can extract information e.g. about the crystal structure, interatomic distances, the distribution of the electrons and, as done in this work, one can investigate how these observables change after laser excitation on a time-scale of the atomic motion.

2.1.1 Fundamentals of X-Ray Diffraction

Bragg-Reflection and Laue's Equations

First we will consider monochromatic x-rays scattering from an 1-dimensional arrangement of point-like scatterers. Like in the diffraction theory of optical wavelengths constructive interference of the scattered waves lead to an intensity maximum where destructive interference leads to an intensity minimum [1]. Constructive or destructive interference occur when the path difference Δs between two scattered waves with the wavelength λ is

$$\begin{aligned} \Delta s &= n \cdot \lambda \quad \longrightarrow \text{constructive interference} \\ \Delta s &= \frac{n}{2} \cdot \lambda \quad \longrightarrow \text{destructive interference} \\ n &= 1, 2, 3, ... \end{aligned} \tag{2.1}$$

For a case as in fig. 2.1 where the incident x-rays reach the crystal with an angle θ to the lattice planes with a certain orientation (h, k, l) and distance d_{hkl} a small fraction of the incident waves are scattered from each of the lattice planes. We get an constructive superposition of the corresponding x-rays exactly then if *Bragg's law* (2.2)

$$n\lambda = 2d_{hkl} \sin\theta \tag{2.2}$$

is fulfilled. The reflections that result for $n = 1, 2, 3, ...$ are referred to as first order, second order and third order respectively. If the crystal is tilted by the angle θ with respect to the incident x-ray beam different lattice planes (h, k, l) contribute to the reflections. By measuring the angle θ the distance of the corresponding lattice planes can be calculated.

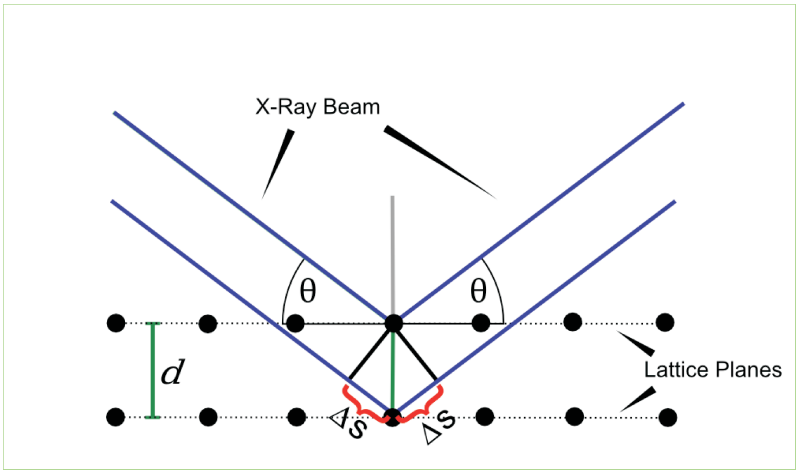

Figure 2.1: Schematic of Bragg-reflection from lattice planes.

An equivalent approach to x-ray diffraction are the *Laue equations*.

For the wave vectors of the incident beam $\mathbf{k}_i = k \cdot \hat{\mathbf{s}}_i$ and the outgoing beam $\mathbf{k}_o = k \cdot \hat{\mathbf{s}}_o$, where $\hat{\mathbf{s}}_i$ and $\hat{\mathbf{s}}_o$ are unit vectors and $|\mathbf{k}_o| = |\mathbf{k}_o| = k$ because only the direction but not the magnitude of $\mathbf{k}$ changes for elastic scattering.

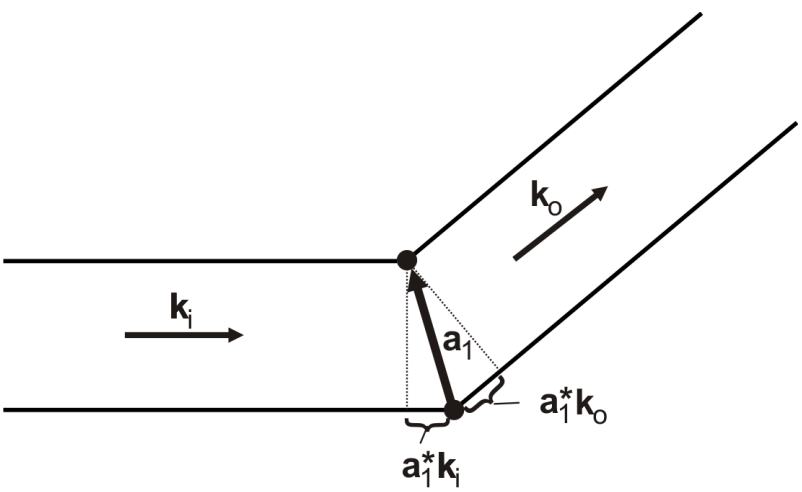

Figure 2.2: Evaluating Laue's equation

If we describe a primitive translation from one lattice point in a crystal to another by a translation vector $\mathbf{T} = n_1\mathbf{a}_1 + n_2\mathbf{a}_2 + n_3\mathbf{a}_3$ then we get a maximum of

intensity for

$$\mathbf{a}_1 \cdot (\hat{\mathbf{s}}_i - \hat{\mathbf{s}}_o) = h_1 \lambda. \tag{2.3}$$

Same follows for the other two space dimensions

$$\mathbf{a}_2 \cdot (\hat{\mathbf{s}}_i - \hat{\mathbf{s}}_o) = h_2 \lambda \tag{2.4}$$

$$\mathbf{a}_3 \cdot (\hat{\mathbf{s}}_i - \hat{\mathbf{s}}_o) = h_3 \lambda. \tag{2.5}$$

These three relations are referred to as the *Laue equations* and can be merged to the relation

$$\hat{\mathbf{s}}_i - \hat{\mathbf{s}}_o = \frac{\lambda}{2\pi} \mathbf{G}. \tag{2.6}$$

$\mathbf{G} = h_1\mathbf{b}_1 + h_2\mathbf{b}_2 + h_3\mathbf{b}_3$ is a translation vector in reciprocal space and by multiplying (2.6) with $\mathbf{a}_1$, $\mathbf{a}_2$ and $\mathbf{a}_3$ we get back to the *Laue equations* (2.3), (2.4) and (2.5). With the wavevectors of the incident and outgoing x-ray beam beeing

$$\mathbf{k}_i = \frac{2\pi}{\lambda} \hat{\mathbf{s}}_i \quad \text{and} \quad \mathbf{k}_o = \frac{2\pi}{\lambda} \hat{\mathbf{s}}_o \tag{2.7}$$

equation (2.6) reduces to

$$\Delta\mathbf{k} = \mathbf{k}_i - \mathbf{k}_o = \mathbf{G}. \tag{2.8}$$

Structure Factor

The equations 2.2 and 2.8 only describe the direction in which the X-ray photons will be diffracted. To determine the relative intensity of the diffraction peaks one

must take into account the configuration of the basis of the crystal and the scattering factor of the basis. Given that that X-rays are scattered from the electrons, it is their distribution that determines the diffracted intensity. Due to the rather small effect of the lattice temperature on the diffracted intensity we will not discuss this in further detail here.

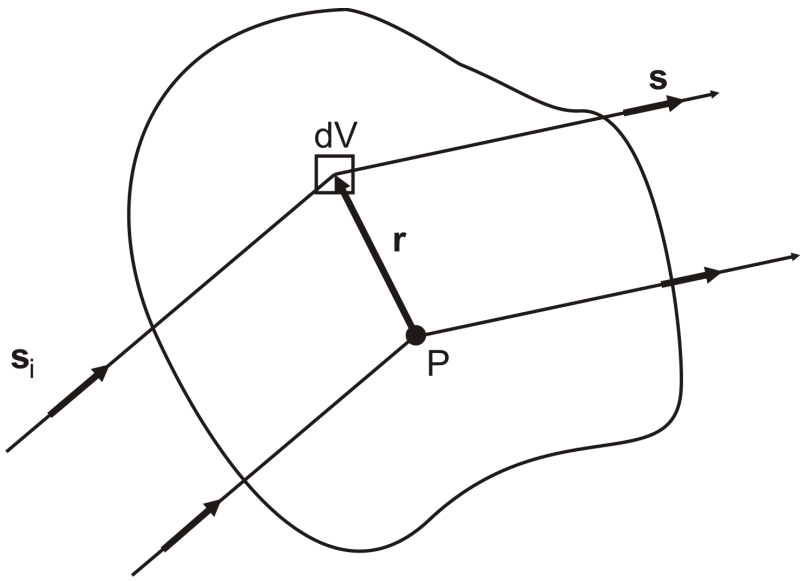

Figure 2.3: Evaluation of the structure factor.

As shown in Fig. 2.3 the path difference of the incident beam with the unit vector $\hat{\mathbf{s}}_i$ scattered in the volume element dV and the beam scattered in the point P have a path difference of $\mathbf{r} \cdot (\hat{\mathbf{s}}_o - \hat{\mathbf{s}}_i)$ with $\mathbf{r}$ being the position vector from dV to P and $\hat{\mathbf{s}}_o$ the unit vector of the scattered beam. The phase difference $\varphi(\mathbf{r})$ between the incident and the scattered wave is then

$$\varphi(\mathbf{r}) = \frac{2\pi}{\lambda}\mathbf{r} \cdot (\hat{\mathbf{s}}_o - \hat{\mathbf{s}}_i). \tag{2.9}$$

Now the the amplitude of the electric field of the light wave scattered from a crystal with the electron distribution $n(\mathbf{r})$ is proportional to

$$\begin{aligned} F_{hkl} &= \int_V n(\mathbf{r}) \cdot \mathrm{e}^{\frac{2\pi i}{\lambda}\mathbf{r}\cdot(\hat{\mathbf{s}}_o - \hat{\mathbf{s}}_i)} dV \\ &= \int_V n(\mathbf{r}) \cdot \mathrm{e}^{i\,\mathbf{G}\cdot\mathbf{r}} dV \end{aligned} \tag{2.10}$$

Because reflections can only occur in the directions defined by Laue's Eq. 2.8 we substituted $\frac{2\pi i}{\lambda}\mathbf{r}\cdot(\hat{\mathbf{s}}_o - \hat{\mathbf{s}}_i) = \mathbf{G}$ in Eq. 2.10. F_{hkl} is called the *structure factor* and is equivalent to the Fourier-transform of the scattering electron distribution $n(\mathbf{r})$. Just as $\mathbf{G}$, F_{hkl} also depends on the Miller indices (hkl).

If we now define $\mathbf{r}_j$as the position vector from the center of the atom at P to the center of another basis atom j and $\mathbf{R}$ as the position vector from the center of the basis atom to a volume element of the electron shell we can write $\mathbf{r}$ from Eq. 2.10 as

$$\mathbf{r} = \mathbf{r}_j - \mathbf{R} \tag{2.11}$$

and substituting $\mathbf{r}$ in Eq. 2.10 leads to

$$F_{hkl} = \sum_j \mathrm{e}^{i\,\mathbf{G}\cdot\mathbf{r}_j} \int_V n_j(\mathbf{R}) \cdot \mathrm{e}^{i\,\mathbf{G}\cdot\mathbf{R}} dV. \tag{2.12}$$

Now we can split up Eq. 2.12 in a factor for the lattice and a factor for for the electron distribution of each lattice atom j

$$f_j = \int_V n_j(\mathbf{R}) \cdot \mathrm{e}^{i\,\mathbf{G}\cdot\mathbf{R}} dV \tag{2.13}$$

which is called the *atomic scattering factor* for the basis atom j. If all the electrons of the basis atom j were located at $\mathbf{R} = 0$, the center of the atom, then the atomic scattering factor would be equal to the atomic number Z and it decreases the more the electrons are distributed [1].

Rocking Curves

Bragg's law (and also the Laue-equation) seem to suggest, that a monochromatic (collimated) beam incident onto a crystalline sample will be diffracted only when

the angle of incidence equals exactly the Bragg-angle. This is actually not the case and the diffraction intensity as a function of the angle of incidence (the so-called rocking curve) always exhibits a finite angular width. This finite width is caused by the finite number of scatterers which effectively contribute to the diffraction signal.

Here two cases need to be discussed. In the first (simpler) case the sample is sufficiently 'small' (e.g. a thin film) so that attenuation of the incident beam due to scattering (extinction) or photoelectric absorption can be neglected. This is called 'kinematic approximation' and the shape of the rocking curve of a particular Bragg-reflection is essentially given by the Fourier-transform of the sample shape. When the samples are 'large' and extinction and absorption cannot be neglected the so-called 'dynamic' diffraction theory must be applied. It takes into account attenuation of the incident wave and the fact that the intensity of the scattered wave becomes comparable to the intensity of the incident wave. In the 'dynamic' case attenuation limits the number of lattice planes which contribute to the diffraction signal resulting in a small but finite width of the rocking curve [2].

To illustrate this effects Fig. 2.4 shows calculated rocking curves, using the software package XOP [3], of the symmetric (001)-Bragg reflection of the ferroelectric material $Pb(Zr_{0.2}Ti_{0.8})O_3$ (PZT 20/80) for the case of a 100 nm thin film (blue) and a bulk (semi-infinite) crystal (orange). The film exhibits a much wider rocking curve (approx. 0.073°) than the bulk crystal (0.0078°) because the extinction depth (absorption is negligible in this case), which determines the width of the rocking curve for the bulk crystal, is 2 µm and thus much larger than the 100 nm thickness of the film. Thus for the film the kinematic approximation is valid and the rocking curve represents essentially the square of the absolute value of the Fourier-transform of the sample shape. Along the (001)-direction (surface normal) this is a rectangle and its Fourier-transform is the sinc-function. This simple consideration explains the appearance of the secondary interference maxima, the so-called thickness fringes. Measuring the angular spacing $\Delta\vartheta$ of the thickness fringes represents an easy way to determine the thickness of thin films using X-ray diffraction [4]:

$$d = \frac{\lambda}{3 \cos \vartheta_{Bragg} \cdot \Delta\vartheta} \tag{2.14}$$

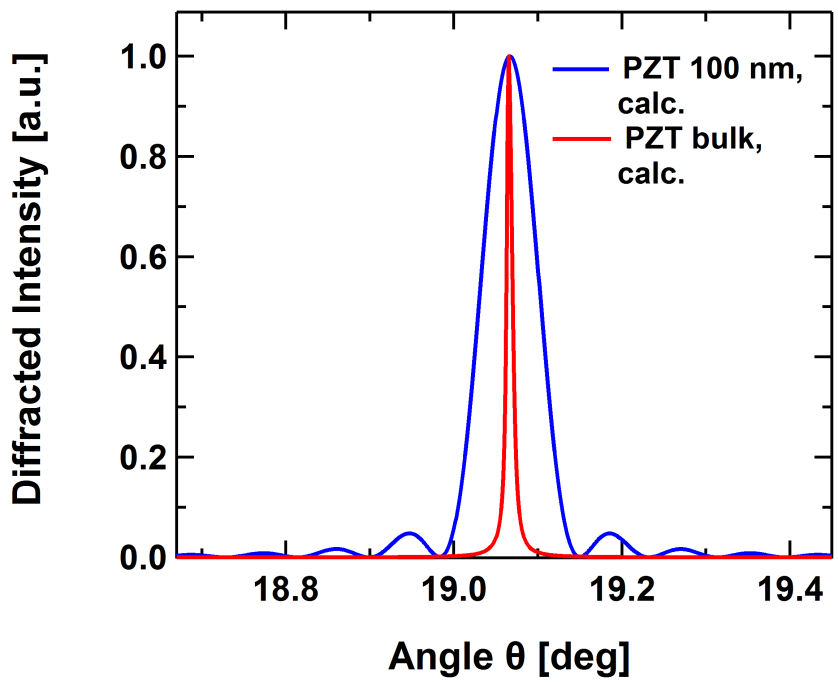

Figure 2.4: A comparison of rocking curves from (001) PZT: The orange curve is a calculated curve from a bulk crystal; the blue line a calculated curve for a 100 nm film and the red curve is a real rocking curve of a 100 nm thin film sample used in this study.

It should be noted that in a real diffraction experiment other factors can contribute the width and shape of the rocking curve: A polychromatic and/or divergent X-ray beam and sample imperfections (e.g. mosaic crystals, defects, imperfect interfaces in thin film samples) will widen the measured rocking curves and may, for example wash out the thickness fringes. Examples will be discussed amongst others in Chapter 4.2.1.

2.1.2 Optical Pump - X-Ray Probe Experiment

As already mentioned earlier, X-ray diffraction is not only a a powerful tool to look at the static structure of crystals but also to investigate the transient changes occurring in a crystal lattice after inducing a certain process.

Therefor optical pump - X-ray probe experiments use an ultra-short laser pulse to excite (pump) by depositing energy in the sample under investigation while an ultra-short x-ray pulse is used to observe (probe) the changes in the lattice structure triggered by the laser pulse. The term ultra-short here refers to the temporal duration (the full width at half maximum, FWHM) of the light pulse and is in the sub-picosecond range. This is necessary if one wants to time-resolve atomic motion which is in the sub-picosecond regime (typical phonon frequencies are of order of 10^{12} - 10^{13} s^{-1}).

The pump-probe experiment at the Universität Duisburg-Essen (UDE) for example, described in Chapter 3.9, uses a laser pulse with a duration of 100 fs and a X-ray pulse of the same order of magnitude. For the experiment at the LCLS in Stanford, USA (see Chapter 3.1.2) laser pulses of 40 fs FWHM and X-ray pulses of 60 fs were used.

Due to the lack of detectors fast enough to resolve the measurable changes in the observed X-ray diffraction signal the time-resolution at these time-scales is achieved by using a trick known as *pump-probe*: One of the beams is sent over a path of variable length while the path of the other beam stays constant. By changing the path s of one of the beams by Δs, the arrival time of the light pulses is delayed relatively to one another by the time $\Delta t = \frac{\Delta s}{c}$ the light takes to travel the path difference at the speed of light c. By reading out the detector for every time-step one gets a chronological succession of diffraction patterns along the observed process.

2.1.3 Effects of Optical Excitation

Irradiating a solid with ultra-short intense laser pulses allows to deposit a controllable amount of energy almost instantly in the system. At first the energy of the light pulse is deposited by exciting the electronic subsystem. Within the electronic subsystem the energy usually thermalizes very rapidly on a time-scale of 10s of femtoseconds. Subsequently the 'hot' electrons transfer their excess energy to the crystal lattice via electron-phonon interactions on a typical time-scale of a few ps. On the same time-scale electronic transport processes (diffusion) may transport the energy into the depth of the material.

This ultra-fast energy deposition causes an immediate increase of stress within the material due to the impulsive temperature increase before the volume of the system changes causing pressure (thermal expansion of the lattice). Due to the equilibrium of forces between the lattice components inside the material the expansion of the lattice starts at the interfaces. This lattice expansion now starts to propagate through the material forming an so-called acoustic wave. This acoustic (expansion-) wave leads to a relaxation of the pressure throughout the material. These waves can be considered as a coherent superposition of phonon modes [5, 6].

Materials such as ferroelectrics, which will be studied in more detail in this work, exhibit unlike most other materials, a negative thermal expansion coefficient. This means that after optical excitation with femtosecond laser pulses a negative pressure builds up inside the material leading to the formation of a compressive wave that propagates through the material.

To estimate the timescale of how long it takes for such an acoustic wave to travel through a thin film one can calculate the ratio of the speed of sound v_s and the thickness d

$$\tau = \frac{v_s}{d}. \tag{2.15}$$

The typical timescale for such waves in thin films of ≈ 100 nm length is of tens of picoseconds for typical sound velocities of a few kilometers per second.

2.2 Ferroelectrics - Structure and Basic Properties

Ferroelectric materials have been known since the beginning of the 20th century when Valasek discovered that the orientation of electric polarisation of sodium potassium tartrate tetrahydrate $NaKC_4H_4O_6 \cdot 4\ H_2O$, also known as Rochelle salt, could be switched to the opposite direction by application of an external electric field. But as Rochelle salt has a very complicated structure one was still far from understanding the phenomenon. It stayed the only known example of this kind and scientific interest was little. After discovering KDP (potassium dihydrogen phosphate, KH_2PO_4) about a decade later, which also showed ferroelectric effects it took until 1945 until the ceramic barium titanate ($BaTiO_3$) was dicovered on a systematic search for new dielectrics to replace mica. Barium titanate with its perovskite structure (see also section **??**) became the most extensively investigated material with ferroelectric properties. This led to the discovery of a large number of further ferroelectric materials with a perovskite structure for example $LiNbO_3$, $PbTiO_3$ or $Pb(Zr_xTi_{1-x})O_3$. Until today many questions concerning the origin of these effects and their transient behavior remain unsolved and are still subject to intense research.

2.2.1 Polarization & Ferroelectricity

Polarization

For an electric charge q separated by the position vector $\mathbf{r}$ the dipole moment $\mathbf{p}$ is

$$\mathbf{p} = q\,\mathbf{r}. \tag{2.16}$$

The polarization $\mathbf{P}$ is defined as the sum over all dipole moments

$$\mathbf{P} = \sum q_n \mathbf{r}_n \tag{2.17}$$

where $\mathbf{r}_n$ is the position vector of the charge q_n [7]. $\mathbf{P}$ describes the dislocation of charges by applying an external electric field $\mathbf{E}_0$. Every atom in the material subject to the field becomes a dipole.

For an externally applied electric $\mathbf{E}_0$ the average field $\mathbf{E}(\mathbf{r}_0)$ at a lattice point $\mathbf{r}_0$ equals

$$\mathbf{E}(\mathbf{r}_0) = \frac{1}{V_c} \int \mathbf{e}(\mathbf{r}) dV \tag{2.18}$$

by averaging over the volume V_c of the crystal cell for an microscopic dipole field $\mathbf{e}(\mathbf{r})$. The contribution of the polarization to the macroscopic field of the homogenously polarized system can be seen as if it were produced by the fictive charge density $\sigma = \hat{\mathbf{n}} \cdot \mathbf{P}$ then the field produced by the polarization is

$$\mathbf{E}_1 = -\frac{\sigma}{\epsilon_0} = -\frac{\mathbf{P}}{\epsilon_0} \tag{2.19}$$

Then the macroscopic electric field of the polarized body can be written as

$$\mathbf{E} = \mathbf{E}_0 + \mathbf{E}_1 = \mathbf{E}_0 - \frac{\mathbf{P}}{\epsilon_0}. \tag{2.20}$$

$\mathbf{E}_1$ is called *depolarization field* as it counteracts with the external field $\mathbf{E}_0$ inside the body [7, 8].

Ferroelectricity

Ferroelectric crystals also exhibit an electric dipole moment without an externally electric field. Usually this so-called *spontaneous polarization* is temperature dependent and vanishes above a certain transition temperature called the *ferroelectric*

Curie-temperature T_C due to its analogy to the magnetic Curie-temperature. Above T_C the crystal goes from its ferroelectric state into the *paraelectric* state. There the length of c-axis parameter of tetragonally distorted unit cell decreases until the cell has reached a cubic structure. Thus the positive and negative charges move together until the dipole moment vanishes.

The length of the c-axis and thus also the polarization are also coupled to the other axes of the unit cell. This is the reason why the ferroelectric behavior of thin films, where the in plane lattice constants are determined by the underlying substrate, differ significantly from bulk materials. This will be discussed in more detail later.

Crystal Structure

A large class of ferroelectric crystals are oxide crystals with a *perovskite* structure as for example lead titanate ($PbTiO_3$, PTO). Fig. 2.5 shows the structure of PZT. Above T_C the Ti^{4+}, Pb^{2+} and O^{2-} ions form a centrosymmetric cubic structure. Below the Curie-temperature of about 470°C the Ti^{4+} ions are slightly displaced with respect to the O^{2-} ions giving rise to an electric dipole moment. At the same time the unit cell is tetragonally distorted. The length of the c-axis (i.e. polarization direction) is strongly coupled to the magnitude of the polarization. I would like to stress that this is the reason why in the experiments discussed in this thesis, measurments of the changes of the c-axis-length by time-resolved X-ray diffraction can provide information about the laser-induced polarization dynamics. Moreover, the polarization is sensitive to external stimuli like changes in temperature and pressure, and, as will be discussed in the presentation of the experiments, by optical excitation.

Ferroelectric Domain Structure

In a ferroelectric material with a spontaneous polarization the polarization is divided into many small *domains* in each of which the direction of polarization is constant.

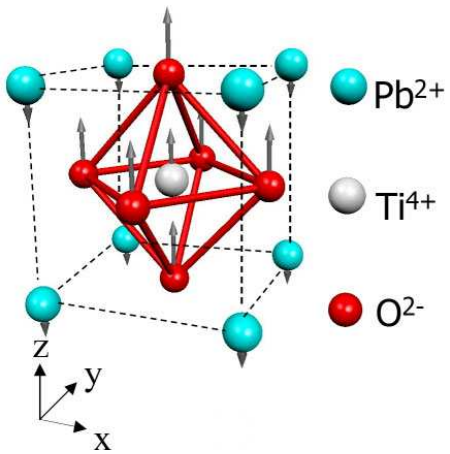

Figure 2.5: Crystal structure of the lead titanate ($PbTiO_3$, PTO) unit cell. The grey arrows indicate the direction in which the respective ions are displaced. SOURCE: Qi [9].

In order to reduce the energy of the external field **E** of a ferroelectric crystal the polarization direction of the individual domains are arranged in such a way that the net total polarization of the whole material is minimized (Fig. **??**).

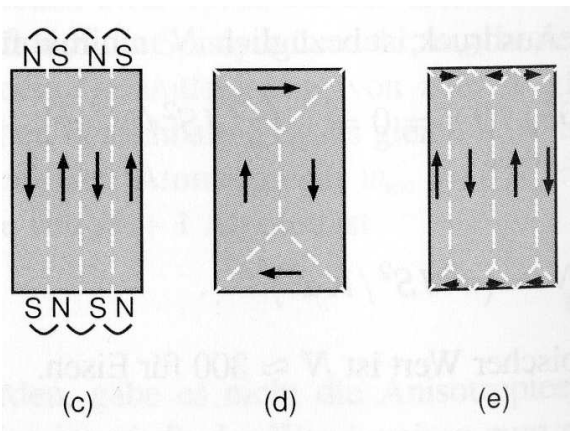

Figure 2.6: Schematic how minimizing an external magnetic or electric field by forming domain works. (a) four domain configuration with external field, (b) four domain configuration with less external field, (c) ten domain configuration with least external field. SOURCE: Kittel [7].

By forming two opposite domains the electrostatic energy can be reduced by

about one-half, and can be decreased further by forming even more, smaller domains. This phenomenon although, works against the energy it costs for the domains to build up domain walls in which the direction of polarization must be alternated. These are called *Bloch-walls*. The energy to rotate the polarization from one unit cell to another to the opposite direction would cost to much energy. Therefore the polarization direction is rotated gradually over a number of unit cells (Fig. **??**). By applying an external field to such a crystal, the domains with their polarization oriented parallel to the direction of the field grow while the domains of opposite direction shrink until the field is large enough to form a single domain and the whole material is polarized parallel to the field [7, 8].

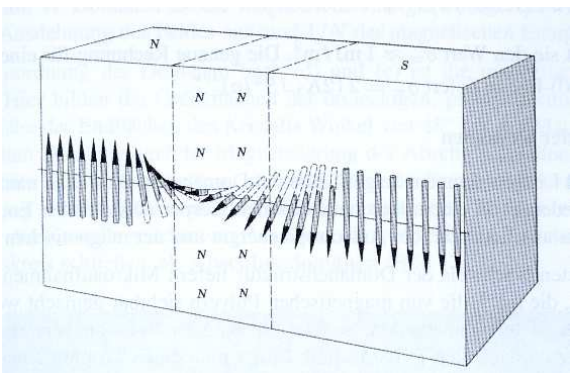

Figure 2.7: Demonstration of Bloch-wall on equivalent example of magnetic domain wall. SOURCE: Kittel [7].

Chapter 3

Experimental Setups

The experiments presented in this work were carried out at two significantly different X-ray sources used for X-ray diffraction experiments: The Linac Coherent Light Source (LCLS), an accelerator based Free Electron Laser (FEL) operating in the hard X-ray regime up to photon energies of 10 keV and pulse durations down to 5 fs, and a laser-plasma based souce using the characteristic 4.51 keV K_α radiation of the target material Titan (Ti) at a pulse duration of a few hundred femtoseconds. The following Section 3.1 and 3.2 will explain their basic principles and properties in more detail.

Another important part of this work was to upgrade the experimental setup at the Universität Duisburg-Essen (laser-plasma-source) to implement new features needed for carrying out certain experiments on lead zirconate titanate thin films [$Pb(Zr_{0.2}Ti_{0.8})O_3$, PZT]. More information on these samples and the results see Chapter 4. Additionally concepts were worked out and partially put into action to fully automatize the experimental procedure. Goals of these upgrades were to improve the flexibility, reproducibility and efficiency of the whole experiment. More about this below in section 3.3.

3.1 Linac Coherent Light Source in Stanford, USA

The LCLS is located at the SLAC National Accelerator Laboratory in Menlo Park, USA and is operated by Stanford University for the U.S. Department of Energy. The LCLS is partly constructed from 1/3 of the original 3 km long linear accelerator at SLAC formerly used for particle experiments. The construction of the LCLS began in the year 2005 and first lasing was achieved in 2009.

This 4th generation light source has the highest peak brilliance of all present X-ray sources of $> 10^{33} \frac{\text{Photons}}{\text{mm}^2 \cdot \text{mrad}^2 \cdot \text{s}}$ in 0.1% bandwidth and is the only FEL in the hard X-ray regime at the moment. Fig. 3.1 shows a comparison of the peak brilliancies of different light sources already operating or under construction (e.g. European XFEL is still under construction and FLASH (seeded) merely planned) where the Ti-K_α laser-plasma source with its peak brilliance of $\approx 10^{18} \frac{\text{Photons}}{\text{mm}^2 \cdot \text{mrad}^2 \cdot \text{s}}$ is denoted by the red circle.

3.1.1 Principle of the LCLS Free Electron Laser

In principle a X-ray FEL produces light pulses by accelerating electrons up to relativistic energies in a linear accelerator, compressing them to ultrashort pulses and then sending them through a long undulator, where the electrons are forced to emit X-rays. This principle is illustrated in the schematic in Fig. 3.2.

In the electron gun a laser, synchronized to the radio frequency of the accelerator modules, illuminates a cathode where electrons are emitted by photoemission. This electron pulse with a typical bunch charge of 20 - 250 pC and a pulse duration of 3 - 6 ps , respectively [11] is injected into the linear accelerator (Linac) and accelerated to an energy up to 15 GeV and an energy spread < 0.01 % and emittance of < 12 pm·rad [12]. Emittance is defined as the product of RMS spot size and RMS opening angle and is an important parameter for a high quality electron beam as needed for an FEL. Before entering the long undulator (i.e. 122 m at the LCLS) the electrons pass a bunch compressor to compress the pulse to the desired duration.

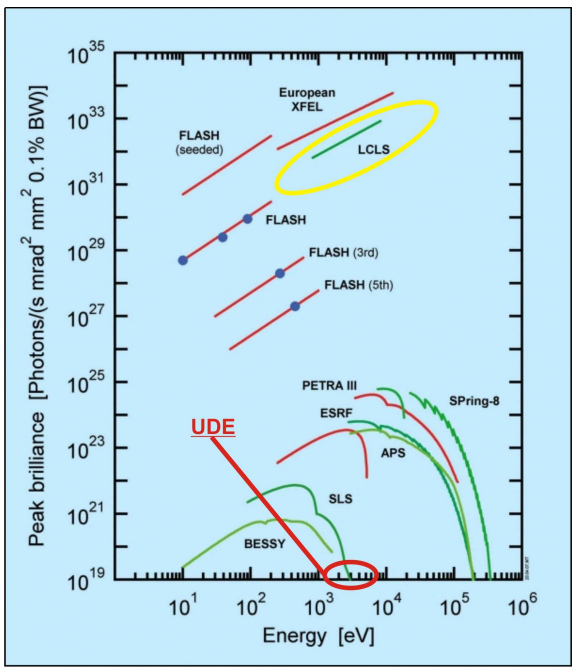

Figure 3.1: Comparison of the peak brilliancies of different lightsources. The position of the laser-plasma-source at the Universität Duisburg-Essen (UDE) is marked by the red circle, the LCLS by the yellow circle. Source: DESY *[10]*

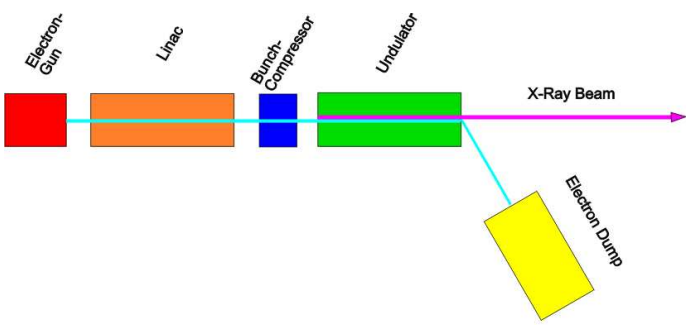

Figure 3.2: Schematic of an FEL with its basic components

Now this beam passes the undulator which is a periodic arrangement of alternating magnets with a periodicity λ_w (see Fig. 3.3) where the electrons are forced to

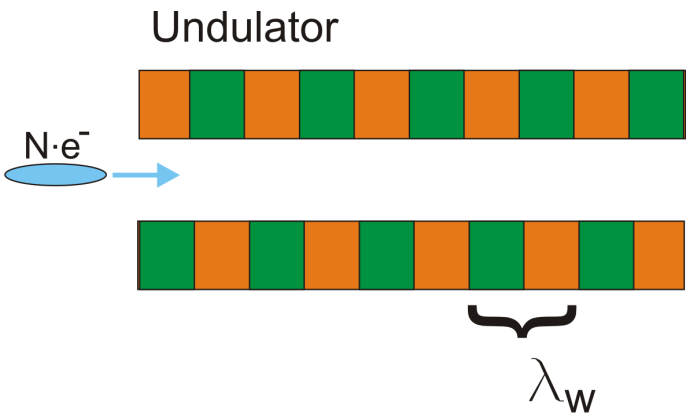

Figure 3.3: Schematic of an undulator with an incoming electron bunch (blue) and the undulator period λ_w. The alternating magneting poles are symbolized as green and orange blocks.

a nearly sinusoidal motion caused by the Lorentz force. Due to this motion the electrons traveling with the velocity v start emitting synchrotron radiation of the wavelength [11]

$$\lambda = \frac{\lambda_w}{2\gamma^2}\left(1 + \frac{K^2}{2}\right) \tag{3.1}$$

$$\text{with} \quad \gamma = \left(1 - \frac{v^2}{c^2}\right)^{-1/2}. \tag{3.2}$$

The term $\frac{K^2}{2}$ with $K = 0.93 \cdot B \cdot \lambda_w$ results from the reduction of the velocity of the electron in z-direction due to the transverse deflection by the undulator magnets. This makes it possible to adjust the wavelength of the emitted radiation by changing the peak magnetic field B or the energy of the electrons [12].

At the beginning of the undulator the synchrotron radiation emitted by the electrons is incoherent but after a few meters of travel the electrons start interacting with their own synchrotron radiation. This leads to an energy exchange between the electrons and the co-propagating electromagnetic wave, some electrons are accelerated, others decelerated, and thus to the formation of the so-called microbunches.

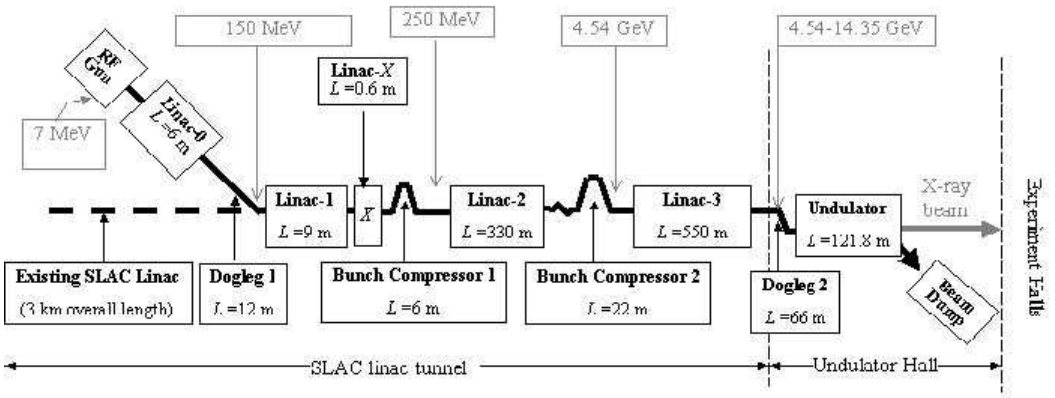

Figure 3.4: Schematic layout of the LCLS showing the energies of the electron beam at stages of the linear accelerator. Bunch compressors and so-called 'doglegs' compress the bunch of electrons from a peak current of 100 A to 3400 A. Source: *Galayda [13]*

In these microbunches the electrons are spaced by exactly one wavelength of the radiation that led to the bunching. Now the electrons start radiating coherently and constructive interference of the bunch-radiation leads to an exponential growth of the radiation intensity, like in a laser. The resulting increase in brightness, as compared to 'normal' undulator radiation can be qualitatively understood as follows: Due to the coherent superposition of *all* the electron within a microbunch the intensity I of the resulting electromagnetic wave, after traveling through an undulator with N_u periods, is proportional to the square of the number of electrons N_e

$$I \propto N_e^2 \cdot N_u^2. \tag{3.3}$$

On the contrary, in a "normal" undulator without microbunching there is no coherent superposition of the radiation produced by different electrons: the coherent superposition of the radiation of a *single* electron, as for a short undulator used e.g in synchrotron sources where no microbunching occurs, the emitted radiation gains an intensity I

$$I \propto N_e \cdot N_u^2. \tag{3.4}$$

traveling through the undulator. However, it must be noted, that the microbunching starts independently at different positions inside the electron bunch triggered by the initially emitted "spontaneous" undulator radiation. As a consequence the radiation of different microbunched portions is not phase-coherent and the emitted X-ray pulse does not exhibit a smooth envelope but consists of a burst of many independent intensity spikes. Due to the similarity to amplified spontaneous emission in a high-gain laser medium this whole process is called SASE-process (Self-Amplified Spontaneous Emission)

Fig. 3.5 demonstrates the SASE-principle and shows schematically the evolution of the electron bunch as a function of the traveled distance.

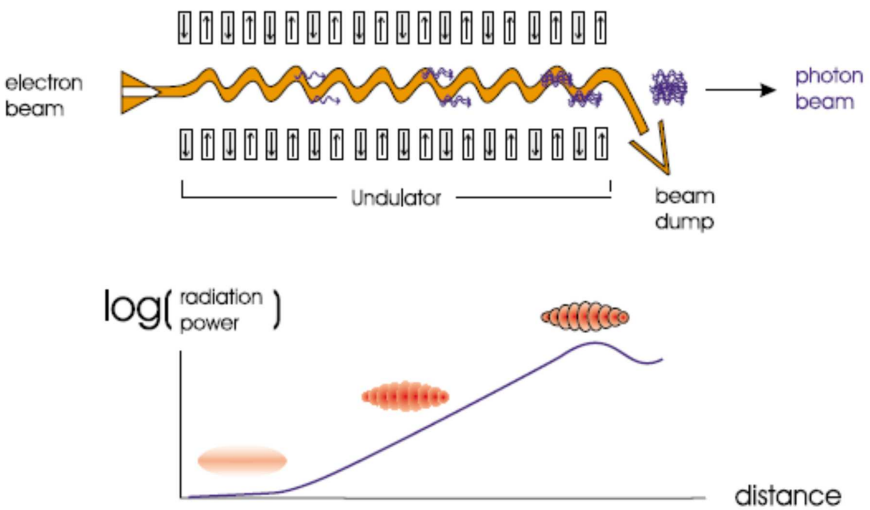

Figure 3.5: This figure schematically shows the SASE process in a long undulator. After traveling a certain distance in the undulator, when the Coulomb-repulsion of the electrons in the microbunches reaches a critical value, no further gain is observed and the pulse duration increases. SOURCE: *XFEL Report [14]*

Due to the fact that the motion of the electrons in the undulator isn't a perfect sinus wave, the spectrum of the emitted radiation contains higher harmonics of the

undulator fundamental λ_u. At LCLS the intensity of 2nd and 3rd harmonic is 1% of the fundamental and provides therefore X-ray pulses up to photon energies of approx. 25 keV (mainly limited by the beamline optics) with intensities which are still very usefull for experiments.

3.1.2 Experimental Setup at the XPP-Station

The LCLS user facility provides a range of different experimental instruments for a large variety of scientific experiments. An overview of the available and planned experimental stations is given in Table 3.1. In this section we will focus on the XPP-station in more detail which was relevant in the experiments presented in this work. For more information see [15].

The X-Ray Pump-Probe (XPP) station at the LCLS is specially designed for carrying out time-resolved pump-probe measurements to study ultrafast structural dynamics in matter. Predominantly a fast optical laser (pulse duration $\approx$ 40 fs FWHM) is used to induce transient states and the hard X-ray pulses provided by the LCLS beam to probe the dynamics triggered by the optical excitation. The x-ray photon energies used here cover the hard X-ray branch from 4 keV to 10 keV in the fundamental and up to 25 keV (2nd and 3rd harmonic).

Optical laser parameters of the Ti:Sa laser-system can be adjusted to individual needs. The fundamental wavelength 800 nm, the 2^{2nd} harmonic (300 nm) such as the 3^{3rd} harmonic (266 nm) are available at pulse energies of up to 20 mJ. The time resolution is in the sub-picosecond regime and is limited to $< 100fs$ RMS by the synchronization between the optical laser and the X-ray pulses.

The core of the XPP station is a configurable diffractometer system which offers great flexibility for mounting samples in a variety of environments, i.e. the water cooled sample heater used for the experiments in Chapter 4.3. The main components are a high precision goniometer and the X-ray detector system.

For detecting the the scattered X-rays the experimental station provides an CCD area-detector and attached to a robotic arm capable of positioning the detec-

Tabelle 3.1: Overview and current status of the instruments available at the LCLS user facility.

Station	Function	Status
AMO *Atomic, Molecular & Optical Science*	Interaction of intense radiation with basic matter	Online
SXR *Soft X-Ray Science*	X-ray emission, absorption & photoelectron spectroscopy	Online
XPP *X-Ray Pump-Probe*	Hard X-rays to probe structural dynamics	Online
CXI *Coherent X-Ray Imaging*	Diffuse scattering and speckle analysis	Online
XCS *X-Ray Coherent Scattering*	Speckle analysis on disordered or modulated materials	Comissioning 2011
MEC *Matter under Extreme Conditions*	Study of transient behavior of matter in extreme states	Comissioning 2012

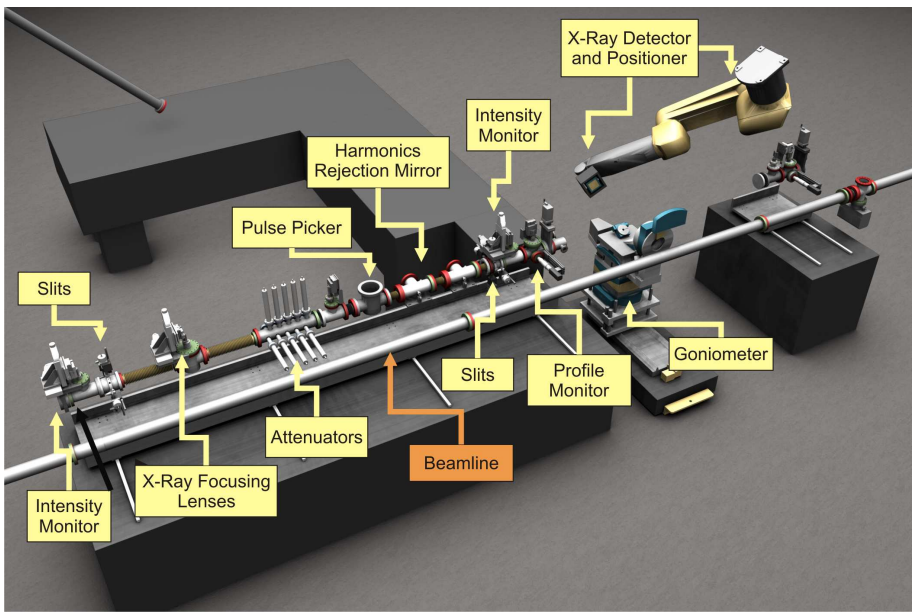

Figure 3.6: CAD drawing of the XPP experimental station with the important components labeled . SOURCE: *LCLS [15]*

tor over a spherical surface with a minimum and maximum radii of 10 cm and 1 m, respectively. This also allows the detector position to be moved remotely from the control room of the experiment while the beam is online. However,for the experiments discussed in Chapter **??** a single channel large area photodiode, also attached to the robot arm (see Fig. 1.7), was used.

The monochromator available at XPP is a so-called channel-cut monochromator designed after the work of Narayanan *et al.* [16] using the Si (111) reflection. It provides an energy resolution of $1.4{\cdot}10^{-4}$ ΔE/E. The monochromator can be moved in and out+++ of the beam and is also appropriate for photon energy scanning measurements.

Other components available at XPP are Beryllium compound refractive X-ray focusing optics and silicon harmonics rejection mirrors but were not used for this work. Further information is available from the LCLS homepage [15] and references given there.

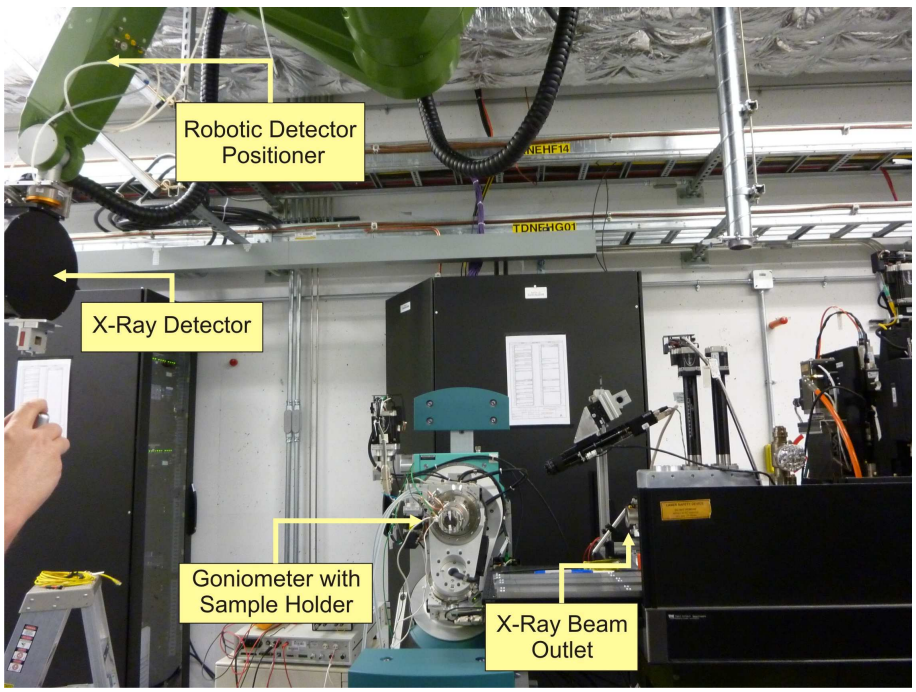

Figure 3.7: Photography of the large area X-ray detector attached to the robotic arm and Huber goniometer

3.2 Laser-Plasma X-Ray Source at Universität Duisburg-Essen

Light sources of the 4^{th} generation, like the X-ray FEL LCLS presented above, are unprecedented in terms of photon flux, beam divergence, pulse duration and many other parameters. Opening a great variety of new scientific possibilities, the LCLS will not stay unique very long - many new 4^{th} generation sources are planned or under construction all over the world [17, 14, 18, 19, ?]. But due to the extensive construction and operational costs as well as the very limited beamtime other X-ray light sources such as laser-plasma based sources remain good alternatives to produce ultrashort X-ray pulses. Their table-top size, low construction costs and their availability make them to affordable solutions for small research groups. But especially for time-resolved optical pump - X-ray probe experiments, they can even

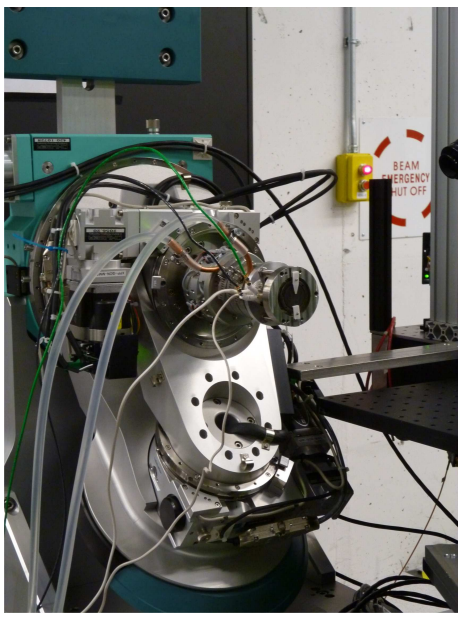

Figure 3.8: Close-up on the Huber goniometer and the water cooled sample heater

compete with large facilities as the LCLS (see also Chapter 4.3).

This section will describe the laser-plasma based X-ray source used for the experiments presented in Chapter 4 and the key components used in the experimental setup.

3.2.1 Principle of Laser-Plasma Based X-Ray Sources

Compared to free-electron lasers, laser-plasma sources represent a completely different approach to produce ultrashort X-ray pulses. A femtosecond laser pulse is focused onto the a solid target at intensities of about 10^{17} - 10^{18} W/cm^2. At these intensities the material in a thin layer at the target surface (approx. 10 nm) is rapidly transformed into a dense hot plasma. Due to the strong electric field of the laser pulse, free electrons from the plasma are accelerated to high kinetic energies (10s of keV). Some of these energetic electron escape from the plasma and penetrate the non-excited material underneath the plasma. A part of these electrons there are decelerated in the electric field of the atoms thereby producing Bremsstrahlung.

If the kinetic energy is sufficient, the accelerated electrons can knock out electrons from the inner shells of the atoms in the solid target material generating core holes. Electrons from higher energy levels will subsequently fill up these vacancies releasing their excess energy by emitting a characteristic X-ray photon. The energy of such a photon is exactly the energy difference between the vacant core hole and the energy level from where the electron falls.

The X-ray energy from such a recombination is a characteristic of the respective atom and the emitted X-ray wavelengths can be changed by using other materials as a target. The characteristic emission coming from transitions from the L-shell to the innermost K-shell is called the $K\alpha$ emission and are usually the strongest X-ray spectral lines. The energies of the $K\alpha_1$ photons from e.g. Titan are 4.51 keV and Copper 8.05 keV.

This characteristic $K\alpha$ line emission and Bremsstrahlung radiation from femtosecond-laser produced plasmas, which results from the interaction of highly energetic plasma electrons with the surrounding material has been well investigated and a more detailed description can be found elsewhere [20, 21, 22, 23].

Due to the dependence of the characteristic line emission on the presence of electrons with energies of about 10 - 100 keV this whole process takes place only during the short time of the laser pulse irradiation and the time-of-flight of the electrons through the target. Consequently the duration of the respective X-ray pulse is of the same order of the plasma producing laser pulse [22].

Important parameters for the efficient production of the short X-ray pulses are for example the laser intensity, the angle of incidence, the shape of the laser pulses, and the plasma parameters and in particular the plasma scale length [24, 21, 25, 26].

3.2.2 Setup of the X-Ray Diffraction Experiment

The laser-plasma X-ray source described in the previous section is used at the Universität Duisburg-Essen to carry out time-resolved X-ray diffraction experiments in an optical pump, X-ray probe configuration. Two different setups are used there of

which one uses the characteristic Ti $K\alpha$ emission line and the other the characteristic Cu $K\alpha$ lines. There are some other significant differences in experimental details of both setups but this work will only discuss the Ti $K\alpha$-setup in more detail.

The X-Ray Source

Laser-plasma based X-ray sources are extremely well suitable for optical pump, X-ray probe experiments with a high time-resolution. On the one hand because of the short pulse durations obtainable which are of the same order as the laser pulses used to produce the plasma and on the other hand there exists no timing jitter between the optical and the X-ray pulse.

The size of the X-ray source in this setup, is approximately 30 µm in diameter as measured by Shymanovich [27], and corresponds approximately to the size of the laser focal spot on the target.

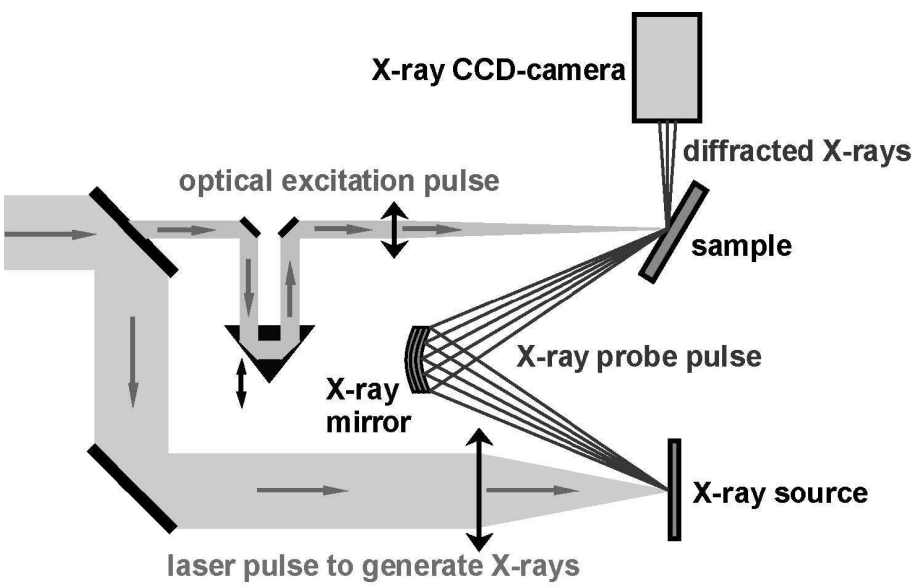

Figure 3.9: Schematic of the optical pump - X-ray probe setup at the UDE. SOURCE: Shymanovich [27]

Figure 3.10 shows measurements of the spectrum of the two characteristic Ti $K\alpha$ lines from the laser-plasma source measured by Shymanovich In this experiment

we use the Ti $K\alpha_1$ line which is realized by using a wavelength selective toroidally

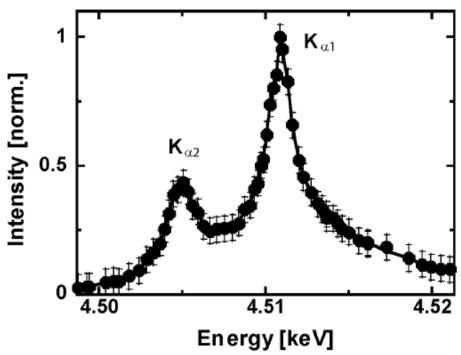

Figure 3.10: Measured spectrum of the Ti $K\alpha$-source at UDE. Source: *Shymanovich [27]*

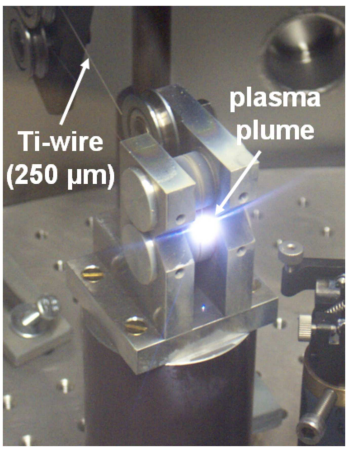

Figure 3.11: Photography of the Ti $K\alpha$-target at UDE in operation. Source: *Shymanovich [27]*

bent mirror described later in this section. The X-ray yield from this source of $\approx 4.5 \cdot 10^9 \frac{\text{Photons}}{\text{Pulse}}$ is also estimated in the section describing the X-ray mirror.

The titanium target for the X-ray production in this setup is technically realized by a special guidance construction for the wire displayed in fig. 3.11 to precisely pull a 250 µm thick Ti wire through the focal spot of the laser. This is necessary, as the surface of the wire is irreversibly destroyed by the laser pulses and the efficient production of X-rays with this source requires a fresh surface for each laser pulse. Using spools with 500 m of Ti wire is enough for 70 h of operation time at a approximate wire speed of 2mm/s. Shymanovich have shown that the position of the wire shifts less than 5 µm during operation which ensures a stable X-ray production.

Details of the Ti Kα Setup

In this section the technical realization of the Ti $K\alpha$ setup will be described. The X-ray source, the sample and the X-ray detectors are all placed in a vacuum chamber of approx. 1 m in diameter at a pressure of approximately 1 mbar. This is necessary

because of the absorption of the Ti $K\alpha$ radiation in air. The transmission coefficient in air is 0.94 fora 1 cm cm path at atmospheric pressure. At an air-pressure of 1 mbar the transmission can be increased to a coefficient of 0.9994 over a path of 1 cm [28]. A further reason for operating the setup in an evacuated chamber is to avoid self-phase modulation of the strongly focused laser beam and ionization of the air leading to distortion of the spatial pulse profile and reduction of the intensity, respectively.

The laser beam is split up into the optical pump beam and the beam for the X-ray generation by a beamsplitter. Then it enters the vacuum chamber through a quartz window and is focused on to the wire target by a lens with a focal length of 30 cm. The X-rays produced on the Ti wire and emitted into the full solid angle are then collected by a toroidal X-ray mirror (described in detail in the next paragraph) and focused onto the sample. The X-ray photons scattered from the sample are then detected by a in-vacuum X-ray CCD-camera which is described in more detail further below in this section. The pump- and probe-beam are nearly collinear; the angle between them is approx. 10°.

The sample holder especially designed for the experiments presented in this work will be introduced in Section 3.3.4. It is mounted on a 5-axis sample manipulator enabling linear positioning of the sample in x-y-z-direction and two rotation axes, one to set the diffraction angle and one to rotate the sample about its surface normal. All these movements are motorized and can remotely be moved while the chamber is evacuated.

X-Ray Optics

Due to the property of a laser-plasma based X-ray source to emit the generated X-rays in to the full solid angle it is necessary to collect as much of the divergent radiation as possible and focus it onto the sample in order to perform X-ray diffraction experiments. This is quite contrary to other X-ray sources such as FEL or

synchrotrons that produce a well collimated beam.

The mirror used here is made of a thin germanium single crystal which is attached to a toroidally shaped thick glass substrate [29]. This kind of mirror uses the reflection of the incident X-rays fulfilling the Bragg condition. Additionally this makes the mirror to an efficient monochromator with a bandwidth of 0.26 eV (see also Table 3.2. Due to the toroidal shape of the crystal the Bragg condition is satisfied at every point of the crystal for the designated wavelength. The ideal shape for a one-to-one point imaging of such a mirror would be elliptical but due to fabrication issues this is hardly feasible. For this reason the toroidal shape is used in a Rowland Circle geometry instead which allows nearly perfect imaging of the point X-ray source [30, 29, 31].

Figure 3.12: Photography of the toroidal Ge mirror attached to the glass substrate. Source: *Shymanovich [27].*

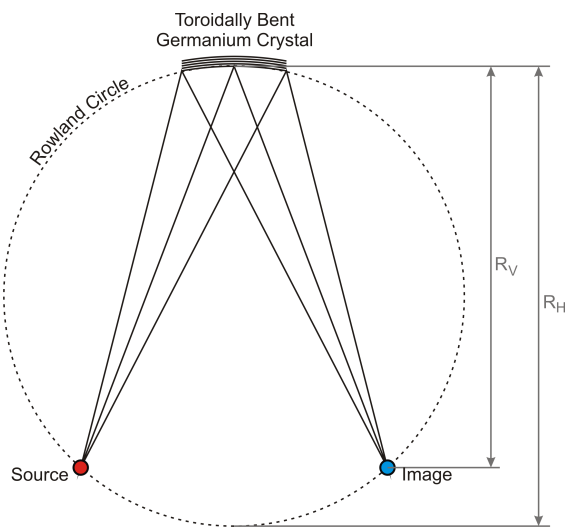

Figure 3.13: Schematic of the toroidal Ge mirror in Rowland geometry. The diameter of the circle equals R_H of the mirror and the distance from the source-image-plane to the mirror equals R_V of the mirror.

In order to achieve the one-to-one point imaging the curvature radii of the mirror must satisfy the condition

$$\frac{R_H}{R_V} = \sin^2 \theta_{Bragg}, \tag{3.5}$$

with R_H being the radius in horizontal and R_V in vertical direction and θ_{Bragg} the Bragg angle for which the mirror is made. Shymanovich have investigated the imaging quality i.e. the spatial X-ray distribution in the topography and in the focal plane of the mirror used in this setup [27]. Table 3.2 shows some of the relevant parameters of the used mirror.

Tabelle 3.2: Relevant parameters of the toroidal Ge mirror used in the Ti $K\alpha$-setup

Crystallographic Orientation	(100)
Orientation Error	$< 10"$
Wavelength	Ti $K\alpha \hat{=}$2.749 Å
Bragg Reflection	(400)
Bragg-Angle θ_{Bragg}	76.4°
Horizontal Radius R_H	498.6 mm
Vertical Radius R_V	473.7 mm
Crystal Thickness	90 µm
Focal Spot Size [27]	70 x 70 µm^2
Bandwidth	$\approx$ 0.26 eV
Diffraction Efficiency	$1.1 \cdot 10^{-5}$
Convergence Angle	$\approx 1.4°$

One can estimate the X-ray yield of the Ti $K\alpha$ source given the total efficiency of the mirror and the X-ray photon flux in the focal spot. Measurements by Shymanovich yield a flux of $\approx 5 \cdot 10^4$ photons per pulse in the focal spot. From this follows a total X-ray yield of the source in to the full solid angle of approximately $4.5 \cdot 10^9$ photons per pulse.

It is worth noting an important detail concerning the convergence angle of the toroidally bent mirror. The convergence angle of the mirror highlighted above is

approximately 1.4°. Offering this angular bandwidth entire rocking curves can be recorded without rotating the sample. Typical rocking-curve widths for thin films we work with are e.g. 0.244° for 100nm FeRh thin films in (100) orientation and 0.09° for 100 nm PZT thin films in(100) orientation (compare to 2.1.1). Furthermore, if the substrate and the film diffraction peak lie close together, as in the case of PZT on STO (more details in Chapter 4.2.1) where the difference of the diffraction angle is about 1.2° they can both be recorded at the same time during a measurement and be used e.g. for calibration purposes. This directly leads to another important advantage of such a large convergence angle of the incident beam concerning time-resolved measurements where e.g. the transient shift of the Rocking curve is observed. Likewise its not necessary to rotate the sample if the shift is less than the convergence angle of the incident X-rays. A sketch of this situation is found in Fig. 3.14.

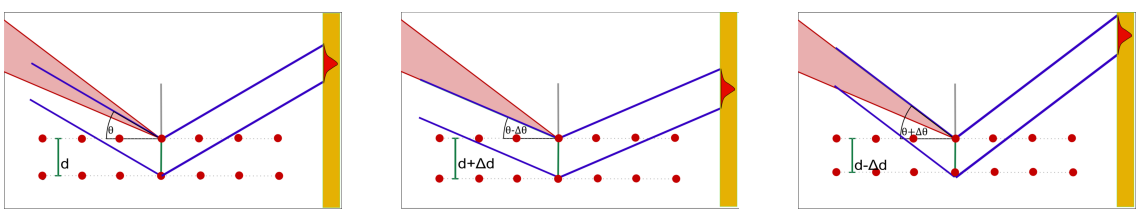

Figure 3.14: Demonstration of the meaning of a convergent incident X-ray beam for a time-resolved X-ray diffraction experiment. The incident cone of X-rays (light red) provides the angles from $\theta - \Delta\theta$ to $\theta + \Delta\theta$ covering a dynamic range of the transient lattice dynamics from a lattice constant $d - \Delta d$ to $d + \Delta d$. The orange bar to the right symbolizes a detector with the shift of the rocking curve (dark red)

Data Acquisition

The X-ray detector used to detect the diffraction signal is a Roper Scientific PI-MTE:1300B in-vacuum X-ray camera with a thinned, back-illuminated Silicon CCD-

chip for low energy X-ray detection. The CCD-chip with a pixel size of 20 x 20 µm and an array of 1340 x 1300 pixel has a quantum efficiency of 55% at 4.51 keV. The camera is cooled down to a temperature of -30°C by a water-cooled Peltier-element to reduce dark current and to allow long exposure times (a few min). To prevent water from condensing and building up ice on the chip this camera may only be used in vacuum. This camera will further be denoted as "**newCam**".

Some additional measures have to be taken to increase the signal-to-noise ratio if working with relatively weak diffraction signals. To prevent optical stray light to contribute to the image background the camera is equipped with a beryllium window. Another problem is the presence of X-ray stray light in the chamber. For this reason a lead-lined nose is mounted on the camera leaving only a small entry hole for the diffracted signal and various lead plates are placed in the chamber to shield the cameras.

Additionally a small GaAs crystal placed close to the source diffracts a part of the produced X-rays onto a second X-ray CCD-camera similar to the "newCam" installed in the vacuum chamber. This signal serves as a reference for the X-ray yield and for normalization of the actual measuring signal. This camera will further be denoted as "**oldCam**"

Laser System

The generation of ultrashort X-ray pulses from a laser-plasma based source requires a laser system that delivers ultrashort und intense laser pulses. The laser system used at the UDE is a Ti:sapphire system based on chirped pulse amplification. The system is described in detail in [30] (and references mentioned there); its main parameters are shown in Table 3.3

Tabelle 3.3: Main parameters of the 10 Hz laser system used for the experiments at the Universität Duisburg-Essen

Laser System	
Type	Mode-locked Ti:Sa
Central Wavelength	800 nm
Repetition Rate	10 Hz
Spectral Width	21 nm
min. Pulse duration	45 fs
max. Pulse Energy	150 mJ
Contrast Ratio at 2 ps	10^{-7}
Beam Diameter (FWHM)	25 mm

3.3 Improvement of the Experimental Setup at UDE

This section will describe technical improvements made to the time-resolved X-ray diffraction experiment presented in Section 3.9. These improvements include automatization of the experimental procedure as well as changes to make it more flexible (pump wavelength, sample temperature). These changes are in particular required for experiments on ferroelectric materials. (see also Chapter 4.1)

3.3.1 Experimental Procedure Before the Improvements

A major drawback of the experimental procedure used so far was the manual and independent operation of its different components. Once the laser system is adjusted and running at operating temperature the vacuum chamber must be evacuated prior to cooling down the X-ray cameras to - 30°C. Performing a time-resolved measurement included the following steps which were carried out manually but could be automatized:

1. Inspection of the pump beam profile and the pump-fluence on an 'old' CCD-

camera and adjustment of fluence with a $\lambda/2$-waveplate and a polarizer.

2. Adjustment of the spatial overlap between optical pump- and X-ray probe-beam. Depending on the sample under investigation and measured variable (shift of rocking curve, change of integrated intensity, broadening or rocking curve, etc) different effects may be used to find overlap. In the case of e.g. FeRh[1] the maximum of the transient shift of rocking curve at certain time-delay is observed.

   (a) Close manual shutters for pump- and probe-beam

   (b) Acquisition of separate background images for *newCam* and *oldCam* without pump or probe beam in the chamber

   (c) Open manual shutter for probe-beam

   (d) Acquisition of a normalization image of the diffraction signal without sample excitation with *newCam* and a reference signal with *oldCam*

   (e) Eventually move delay-stage of optical pump-beam to a delay position with a strong change in the measured variable (depends on sample and magnitude of transient effect)

   (f) Open manual shutter for optical pump-beam

   (g) Acquire image with *newCam* (diffraction signal) and image with *oldCam* (reference signal) simultaneously

   (h) compare measured variable with signal from Step 2d. Difference further denoted as ΔS

[1] Iron rhodium (FeRh) exhibits a structural phase transition from anti- to ferromagnetic at 80°C coupled with a 1% increase of the unit-cell volume. Most of the experiences, concerning the setup and the experimental procedure, were gained in the first 4 months of this work carrying out experiments on FeRh. Experimental results on FeRh mentioned in this work are presented by Quirin *et al.* [32, 33] and references

(i) change vertical or horizontal position of the pump-beam relative to the probe-beam using the micrometer-screws of the mirror that reflects pump-beam into chamber

(j) repeat from Step (2g) until maximum of ΔS is found for one direction (vertical or horizontal), then repeat for other direction.

3. Start of the actual experiment:

   (a) Close manual shutters for pump- and probe-beam

   (b) Acquisition of separate background images for *newCam* and *oldCam* without pump or probe beam in the chamber

   (c) Open manual shutter for probe-beam

   (d) Acquisition of an normalization image of the diffraction signal without sample excitation with *newCam* and a reference signal with *oldCam*

   (e) Move delay-stage of optical pump-beam to the designated delay time between pump- and probe-beam

   (f) Open manual shutter for pump-beam

   (g) Acquire image with *newCam* (diffraction signal) and image with *oldCam* (reference signal) simultaneously

   (h) 3-4x Repetition of Step (3e) to (3g)

   (i) Close manual shutter for pump-beam

   (j) Acquire new normalization image as in Step (3d)

   (k) Repeat Step (3e) - (3j) until time-scan is complete.

   (l) Close manual shutters for pump- and probe-beam.

   (m) Acquisition of separate background images for *newCam* and *oldCam* without pump or probe beam in the chamber.

Similar procedures are also necessary to carry out experiment which investigate the dependence of the diffraction signal as a function of the pump-fluence, (manual variation of the halfwaveplate orientation instead of changing the delay time) or the sample temperature and won't be mentioned separately here. The following section will discuss the measures taken to automatize the individual steps and to integrate them in a single LabVIEW-based control environment. These procedures and integrate them in LabVIEW™ .

3.3.2 Automation of the Experimental Procedure

Automatizing the experiment will have two important effects. First it will considerably reduce the time required to perform a particular experiment. Second, the reproducibility will be enhanced while at the same time the risk of human errors is reduced. The experience from experiments performed so far without automatization shows, that approximately 30% of the total experiment time is used to manually save the acquired images CCD-images, to change the experimental parameters (delay, pump energy, ...) and to start a new acquisition cycle. A 'normal' time-resolved experiment where the delay time is scanned takes usually 8 - 10 hours which could hereby be cut down to 5 - 7 hours.

The general idea of the automatization was to motorize all key components such as the mirror to adjust the spatial overlap and the $\lambda/2$-waveplate to change the pump energy and then integrate all parts, including both X-ray cameras as well as the pump-probe delay-stage in LabVIEW™ .-based control and data acquisition environment.

To make this possible a modular solution was chosen. In this way it was possible to integrate every part separately and be able to control all the parts individually from the same user interface. A central routine, written in the programming language MATlab, is responsible for the connection and communication between all these individually controlled parts. The routine makes the decisions and sends the commands to the corresponding modules.

This design is very flexible, since modules can be added or removed with out the need to reprogram the entire structure and because different modules are shared in different experiments and configurations.

The block diagram in Fig. 3.15 shows as an example the schematic design of the modular LabVIEW™ programm for an explicit time-dependent measurement (e.g. the pump-probe time delay is varied at fixed pump fluence.) of a time-resolved

pump-probe measurement.

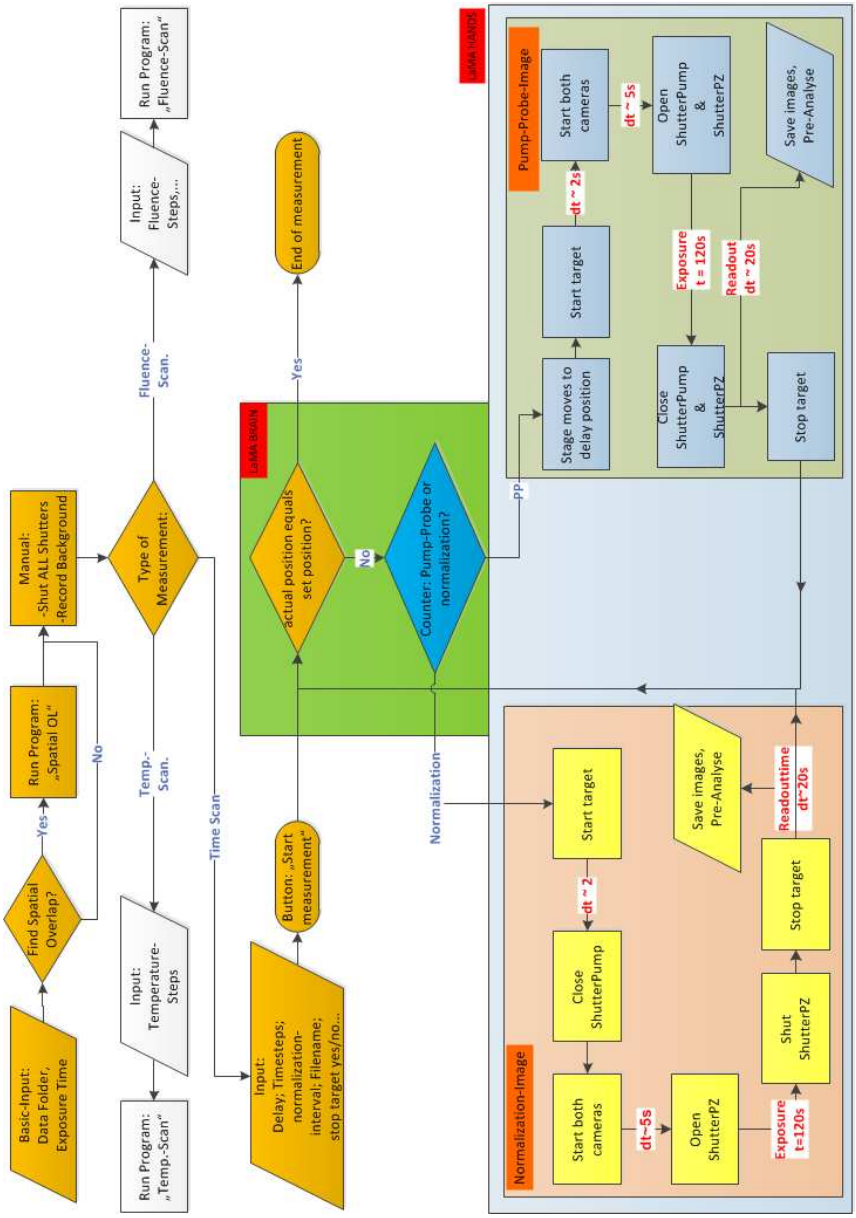

Figure 3.15: Block diagram of the automation programm structure using the example of a time-resolved measurement. The *LaMA Brain* (green box) is responsible for making decisions on what to nest, depending on the procedure (overlap search, time-resolved measurement, pump-fluence dependent, etc.) and the *LaMA Hands* (light blue box) carries out the commands and operates the corresponding modules.

The LaMA Brain and Hands (LaMA: Laboratory Measurement Assistant) are programs written in the programming language MATlab for the convenience of programming more complex case structures than in LabVIEW™ . The LaMA Brain not only makes the decisions on what step is necessary next, but also carries out a pre-analysis of the data by implementing the MATlab program *Automatic-Measure* programmed by Quirin and Shymanovich [33, 27] which is also used as a stand-alone program to analyze the images recorded by the cameras *newCam* and *oldCam*. This is a central function of the routine for searching the overlap since the next decision of the LaMA Brain, wether to continue scanning or stop, depends on the analysis of the last image taken.

Hardware and Software Upgrades

In order to continue with the automatization, some of the components had to be exchanged or additional software and hardware purchased to integrate them in the automatic procedure.

Delay-Stage: The optical delay stage was already motorized by a stepper-motor driven linear translation stage by OWIS. Hardware drivers for LabVIEW™ were delivered with the stage.

Waveplate: The manual rotation stage used to adjust the $\lambda/2$-waveplate is replaced by a stepper-motor driven motorized rotation stage (OWIS DRTM-40).

Overlap Mirror: The mirror used for adjusting the spatial overlap between the optical pump-pulse and the X-ray probe-pulse was, so far, moved by manual micrometer screws with a minimal step size of 5 µm. This corresponds to a step of $\approx$ 56 µm on the sample (The focal spot size of the pump-pulse is $\approx$ 400 µm FWHM compared to a focal spot size of the probe-pulse of $\approx$ 100 µm. The micrometer-screws were replaced by miniature linear stepper-motors (Model Newport NSA12) with an minimal incremental motion of 0.2

µm. This enables a positioning of the pump-beam on the sample in 2 µm steps. LabVIEW™ drivers are included in the system of controller and actuator.

Cameras: Until then the cameras *newCam* and *oldCam* were controlled with the image acquisition software WinView32 from the camera manufacturer Roper Scientific which only allows to control one camera per computer. This means that in order to record an image with both cameras, as necessary during an experiment, the cameras had to be started simultaneously from two different computers. With the purchase of the special software kit SITK® (Scientific Imaging ToolKit™) containing the hardware drivers for LabVIEW™ it became possible to control both cameras with one computer in the same program and integrate them in the overall control routine.

LabVIEW™ Programming

Programming the LabVIEW™ modules for the optical delay stage, the rotation stage for the waveplate and the actuators for the overlap mirror were straight forward and will not be presented here in much detail. Worth mentioning is that much effort was given to ensure full position recovery of all the stepper-motors in operation even after a crash of LabVIEW™ or of the computer or even a power failure. For this purpose a separate file is written *before* each movement of any of the stepper-motors saving the last and next position. This was especially necessary for the mirror actuators NSA12, which lose their position saved in the controller after power loss making it inevitable to do a home search. f From there the last position can be recovered using the function that lets the motors return to their last position. Loosing and recovering the position of the spatial or temporal overlap between pump- and probe-beam can be a time consuming procedure and is essentially important for collecting reproducible data in an experiment.

Implementing X-Ray Cameras in LabVIEW™

Programming a LabVIEW™ -interface for the X-ray cameras was actually one of the most important parts of the whole LabVIEW™ program considering their central role in all measurements. Unfortunately this part turned out to be the most problematic one. Not only because of the more complex nature of image acquisition compared to driving stepper-motors, but also due to problems with the camera driver kit SITK® for LabVIEW™ from Roper Scientific/RCubed Software (RCubed Software Consulting developes software for Roper Scientific products [34]). The SITK® is a collection of hardware drivers, Virtual Instruments for data acquisition and analysis. But compatibility problems, conflicts with program-libraries of older and newer versions and especially the former image acquisition program WinView32 as well as insufficient documentation gave reason to believe that the SITK® is still to be fully developed.

After several weeks of solely attempting to debug the SITK® in close collaboration with SITK® developers from RCubed Software Consulting the program finally was able to simultaneously acquire images from *newCam* and *oldCam* together and then save both in different files with different names according to the measurement procedure and the corresponding measurement step as defined by the LaMA Brain. Final tests of the LabVIEW™ camera interface using the spatial overlap procedure, could't be completed because the .SPE image-files produced by the SITK® lack header information included in the .SPE-files used by WinViw32. This information, containing e.g. the exposure time of the images, the number of pixels etc. is of substantial importance for the data analysis using *Automatic Measure*. Further correspondence with the support of RCubed Software Consulting gave possible solutions for this problem, but couldn't be implemented anymore due to the very limited time available to accomplish this work.

Even though it wasn't possible to make all modules work together yet much advance was made designing the individual modules and the structure of the main

program. Modular programming of these LabVIEW™ measurement routines is a very flexible way to combine different components of a automatic measurement procedure.

3.3.3 Flexible 800/400 nm Pump-Branch

A further step to improve the experimental setup was the design for easily switching the optical pump-beam between the wavelengths 400 nm and 800 nm. Depending on the samples under investigation it can be favorable sometimes to optically pump/excite the sample with a wavelength other than the fundamental wavelength of 800 nm of the laser system. Particularly with regard to the experiments on ferroelectric PZT (see Chapter 4.2) which is nearly transparent for 800 nm but partially opaque for 400 nm according to ellipsometrical measurements of the optical constants in Fig. 4.23.

By second harmonic generation (SHG, or frequency doubling) using a nonlinear crystal one can double the frequency of the 800 nm fundamental wavelength to a wavelength of 400 nm.

Technical Accomplishment

Implementing and adjusting the SHG and especially adjusting the spatial- and temporal-overlap after such modifications can be very time consuming and changes of the excitation wavelength from one day to another are not feasible without further ado. Under these circumstances reproducing experimental parameters can be difficult. For this reason a flexible 400/800 nm pump-branch was designed to gain more flexibility and reproducibility. Fig. 3.16 shows a schematic drawing of the design.

By placing a mirror on to a high precision translation stage one can either move the mirror out of the beam and let the 800 nm beam pass through. Or when the movable mirror is in place, the 800 nm beam is redirected through the

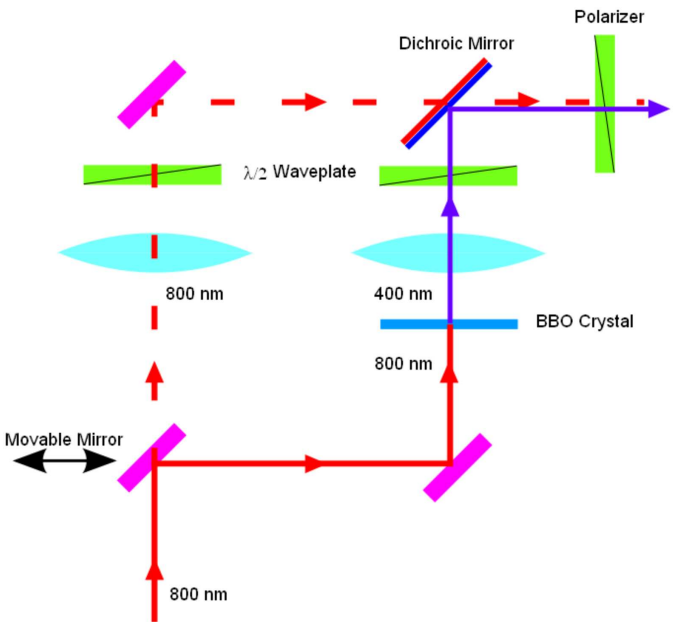

Figure 3.16: Schematic of the flexible 400/800 nm pump-branch.

alternative path where the second harmonic is generated in the non-linear BBO crystal (β-barium borate, β-BaB_2O_3). Due to the wavelength dependency of the $\lambda/2$-waveplate and the focal length of the optical lens, separate components are needed for each branch. To couple the 400 nm beam back into the original path a so-called dichroic beamsplitter (or dichroic mirror) with special dielectric coatings for 400 and 800 nm is needed.

Second Harmonic Generation

To efficiently generate the second harmonic an appropriate non-linear crystal had to be chosen. Due to its high non-linear coefficient, high damage threshold, low temperature sensitivity of the indices of refraction and being only mildly hygroscope a BBO crystal was chosen. For type I phase matching SHG from 800 nm $\rightarrow$ 400 nm in BBO the crystal orientation is $\theta = 29.2°$ and $\varphi = 0°$. Table 3.4 shows the relevant laser parameters needed to calculate the conversion efficiency, the spectrum and the pulse shape of the generated 400 nm laser pulse. The parameter left to choose is the

crystal length, which should be long enough to get a high conversion efficiency but short enough so the spatial profile and the duration of the generated pulse doesn't differ much from the incident 800 nm pulse. Simulations of the SHG done with the non-linear optics simulation programm SNLO [35] show that a crystal length of 150 µm yields a good conversion efficiency with no or only slight changes of the pulse shape.

Tabelle 3.4: Relevant laser parameters for SHG

Laser Parameters for SHG	
Fundamental Wavelength	800 nm
Second Harmonic Wavelength	400 nm
Beam Diameter	$\approx$ 8 mm
Pulse Energy	15 - 20 mJ
Pulse duration	120 fs
Pulse Chirp	8.6 $\cdot 10^{-2}$ THz/fs

Due to lack of time within the limits of this work, the flexible 400/800 nm pump-branch wasn't tested yet. Therefor no measurements were carried out to verify the calculated data to this point. What has to be done is to check the SHG and to perform tests on the accuracy of the switching between the two branches.

3.3.4 New Sample Holder / Heater

A further important task in order to improve the flexibility of the experimental setup and especially make it suitable for experiments on ferroelectric PZT thin films (see Chapter 4.2) is the construction of a new sample holder. In order to also perform experiments on these samples above the ferroelectric to paraelectric phase transition temperature T_C, a new sample holder was designed being capable of heating the sample to a temperature of 800°C. The Curie-temperature T_C of such thin films departs significantly from the bulk value of 470°C due to the influence of the me-

chanical boundary conditions by the substrate [36]. According to measurements by Gariglio *et al.* the transition temperature for the films intended to be investigated is $T_C \approx 680$°C [37].

To reach such high temperatures in such a confined space as in a vacuum chamber where many sensitive components are very close is a challenge that must be well considered.

Even though heat conduction by conduction becomes a negligible factor at a vacuum pressure of about 1 mbar, much attention must be paid to possible issues concerning thermal radiation and heat conduction. Additionally, the sample holder must offer sufficient mechanical stability and feature a low profile due to the very limited space.

Two different types of heater modules were considered and their advantages and disadvantages had to be discussed. The first one is a so-called

Boralectric® Heater: Heater element is a combination of pyrolytic Boron Nitride, a dielectric ceramic material, and pyrolytic graphite, an electric conductor. Ceramic material provides dimensionally and electrical stable heating up to 1800°C and high power density of about 45 W/cm^2. Dimensions: 35.2 mm x 25.0 mm x 3 mm. (Manufacturer: tectra [38]).

Button Heater: Heater with resistance encapsulated in molybdenum body. Heats up to 1200°C in UHV. Dimensions: ∅ 25.4 mm x 33 mm. (Manufacturer: Heat Wave Labs [39]).

Due to the extreme low profile and the mechanical stability the choice was the Boralectric® Heater.

Fig. 3.17 shows a 3D-CAD drawing of the entire heater construction with double tantalum heat shields as it is operating. The total hight of the heater, from the

adapter to the translation stage to the top of the heater element measures approximately 30 mm. A photography of the mounted sample holder can be found in Fig. 3.18.

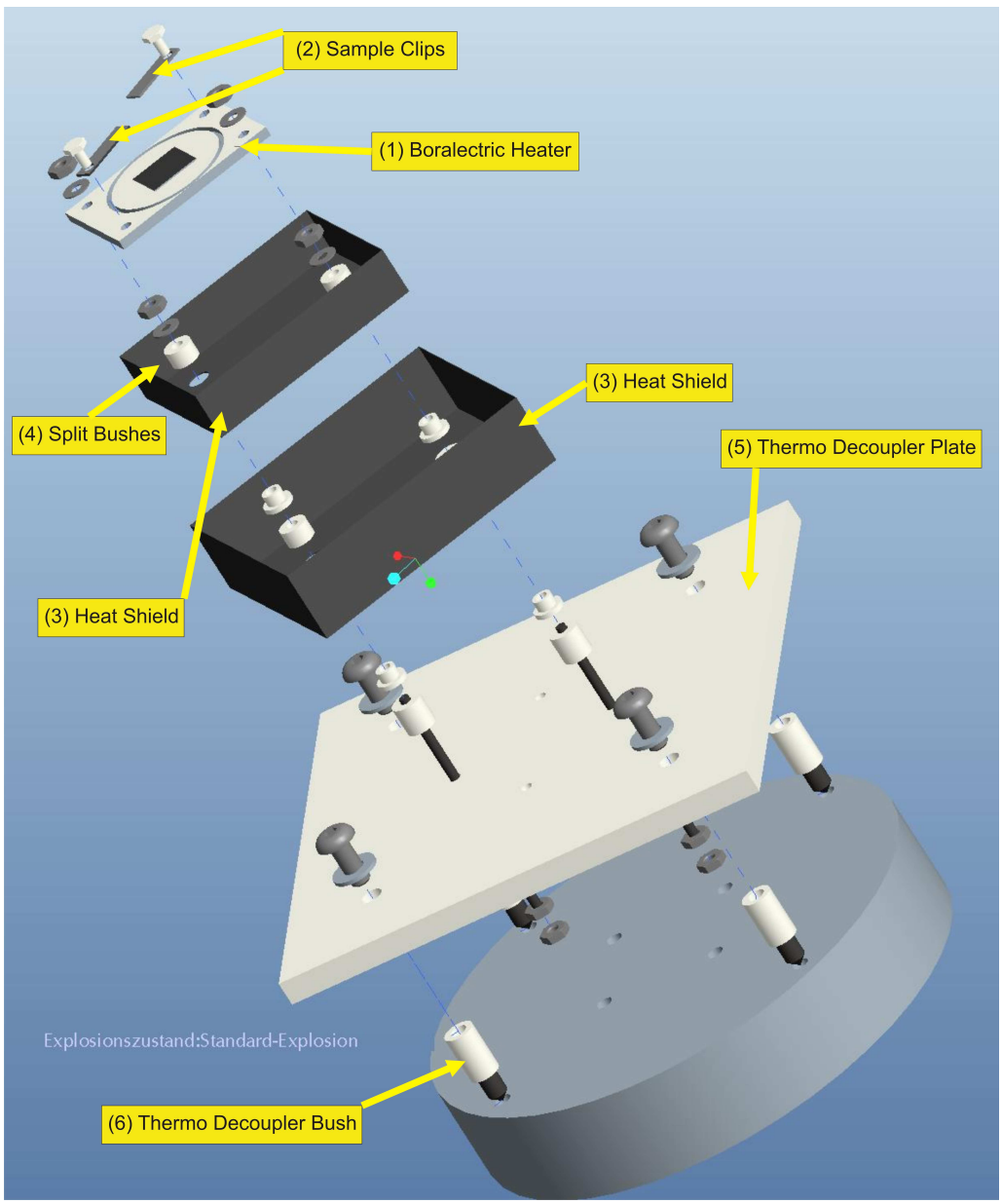

Figure 3.17: Exploded CAD drawing of the new sample holder with the Boralectric heater element.

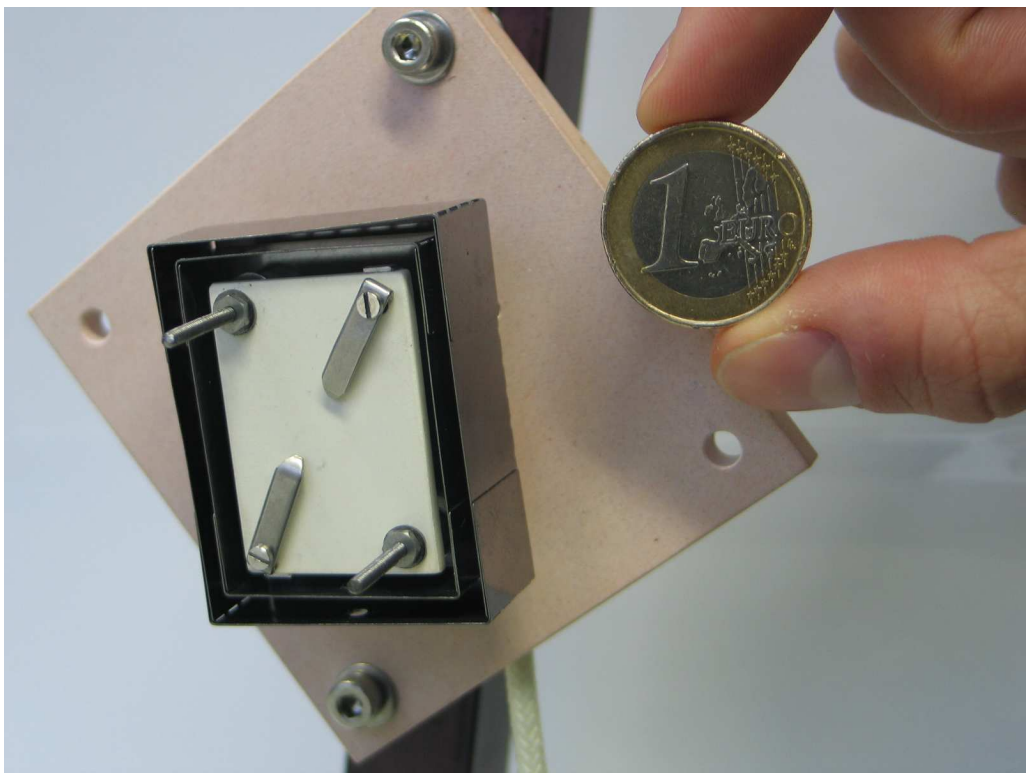

Figure 3.18: Picture of the mounted new sample holder compared to the size of a one euro coin.

To reduce heat conduction from the heater to the translation stage on which the heater is mounted and shield residual thermal radiation the heater is mounted on a sintered alumina plate. Some thermal properties of different ceramic materials are shown in Table 3.5. Despite the difficulties of machining sintered alumina compared to un-sintered ceramics such Macor®, alumina sintered at 1100°C was chosen due to its low thermal expansion coefficient.

To further minimize thermal conduction from the heater to the translation stage, the alumina plate is thermally decoupled from the adapter. Therefor alumina bushes with an internal screw thread were designed allowing to insert a screw from both sides as illustrated in Fig. 3.17. This way a metallic connection can be avoided to minimize heat conduction.

Careful and extensive tests have been performed to test the heater. Mea-

Tabelle 3.5: Thermal Properties of some ceramics. *[40]*

	Thermal Conductivity [W/m °K]	Thermal Expansion Coefficient [10^{-6} K^{-1}]
Alumina, un-baked	1.07	7 - 12
Alumina, 1100°C	1.7	2.9 - 3.6
Alumina, 1300°C	2.2	6-8
Macor	1.46	12.6

surements concerning the surrounding temperature and the temperature at critical points as well as measurements on the thermal stability of the sample holder were performed and are presented in Chapter 4.1.

Chapter 4

Experimental Results

With the continuous development of micro- and nano-technological devices thin films are becoming more and more important for technical applications and have been subject to intense research for many years. From a scientific viewpoint thin films exhibit many new and interesting properties as compared to bulk materials.

Thin films made of ferroelectric materials are of special scientific interest, not only due to their possible technological applications e.g in non-volatile memories [41] but also because of the complex coupling of temperature, strain, polarization and the electronic system they manifest. The 2-dimensional thickness-dependent strain on ferroelectric thin films imposed by the substrate enables ferroelectric properties such as the Curie-temperature or the polarization to be tailored to specific needs [42, 43, 44]. Many questions especially regarding the transient behavior and the speed limits of the effects of such thin film systems still remain open.

The experiments presented in Section 4.2 of this chapter include first tests on the feasibility of time-resolved X-ray diffraction experiments at the Universität Duisburg-Essen (UDE) with ferroelectric $PbZrTiO_3$ (PZT) thin films using the new sample holder. Tests of the new heater are focused on excluding thermal damage of components close to the heater and if the temperatures it was designed for, above T_C, could be reached while ensuring that the required mechanical stability of the heater

is given. Furthermore the PZT samples were characterized using X-ray diffraction under static heating to drive the PZT thin film into the paraelectric phase and compare the observations with other work done on equivalent samples [37, 45].

In Section 4.3, time-resolved optical pump - X-ray probe diffraction experiments performed at the X-ray free electron laser LCLS will be presented. Samples used there were $PbTiO_3$ (PTO) thin film samples on different substrates showing significant differences in behavior depending on the mechanical boundary conditions and temperature.

By applying the techniques of time-resolved X-ray diffraction on ferroelectric thin films we hope to get a deeper insight into the mechanisms connecting the polarization and the lattice strain. Such experiments are mainly motivated by the question, whether and how ultrashort laser-pulses can be used to switch ferroelectric elements and what are the fundamental speed limits.

4.1 Test of new Sample Holder / Heater

After designing and manufacturing the new sample holder described in Chapter 3.3.4 it was necessary to perform various tests as to ensure that the surrounding components in the experimental setup would not be damaged from exposure to the high heat produced by the heater. Further we implemented a setup to monitor the tilt of the sample in dependence of the sample temperature which results from thermal expansion of the mechanical components of which the sample holder was built. The results of these measurements can be found in the following section.

4.1.1 Surrounding Temperature

The use of ceramics with a low thermal conductance and a special construction to decouple the heater itself thermally from the translation stage and the goniometer and the double heat shield behind the heater module were necessary measures to

protect the delicate components of the experimental setup in the vacuum chamber. Due to the low pressure in the vacuum chamber, heat conduction by convection becomes a negligible factor. However, the thermal radiation produced by the heater at the design temperature of 800°C could become a problem. Therefore tests were performed to measure the temperature at various critical positions around the heater.

As described before the temperature of the heater itself was measured by a type K thermocouple (further denoted by **TC1**) in a small hole directly in the heater module. A moveable second thermocouple of the same type (further denoted as **TC2**) was used to monitor the temperature in the surroundings. For the test of the heater the positions of TC2 were chosen as in Table 4.1.

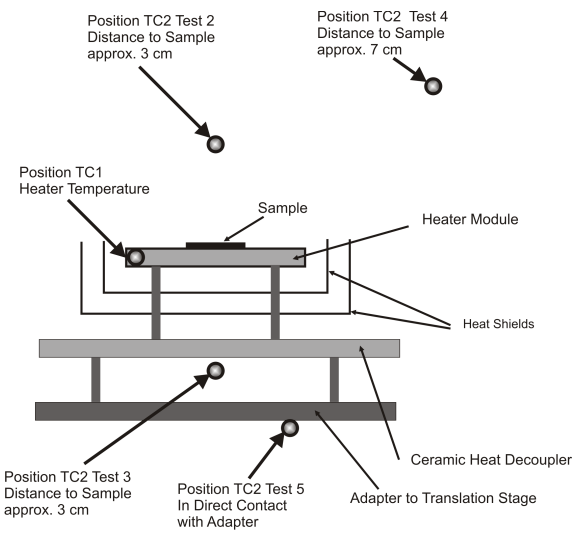

Figure 4.1: Non-scaled schematic sectional drawing of a side view of the sample holder. Also shown are the positions of the two thermocouples TC1 and TC2 to monitor the temperature of the sample and the surroundings.

The results from these measurements are shown in Fig. 4.2. *Test 2* was performed to have a benchmark for *Test 3* where the thermocouple *TC2* was actually placed at the same distance but behind the ceramic heat decoupler. In *Test 3* the Temperature reaches a value of nearly 100°C while the heater is running at a temperature of 600°C (which is 75% of its design value). With the maximum working

Tabelle 4.1: Test series and positions of the thermocouples to monitor surroundings temperature with new sample holder

Thermocouple	Test Series	Position
TC1	n.a.	directly in heater module
TC2	Test 2	3 cm directly in front of heater module / sample
TC2	Test 3	3 cm behind heater module (directly behind heat decoupler)
TC2	Test 4	7 cm diagonally away from heater module / sample
TC2	Test 5	In direct contact with adapter to translation stage

temperature of the translation stage being 50°C, as specified by the manufacturer, a further test series is necessary. This was done in *Test 5* by placing *TC2* behind the adapter plate where the heater is mounted to the translation stage and measuring the increase of temperature after having the heater set to 600°C for approximately 85 minutes. The result presented in Fig. 4.3 shows the that the temperature at the adapter plate doesn't exceed 33°C for this case. Here we concluded that the thermal protection measures for the translation stage are sufficient.

From *Test 4* we see though that it is necessary to take further measures to protect the x-ray CCD camera from thermal damage - especially the plastic foil

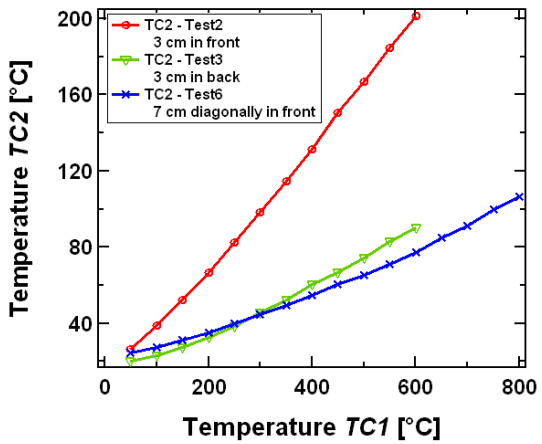

Figure 4.2: Plotted results of the measurements *Test2, Test3* and *Test6.* The line between the measured points is a guide to the eye

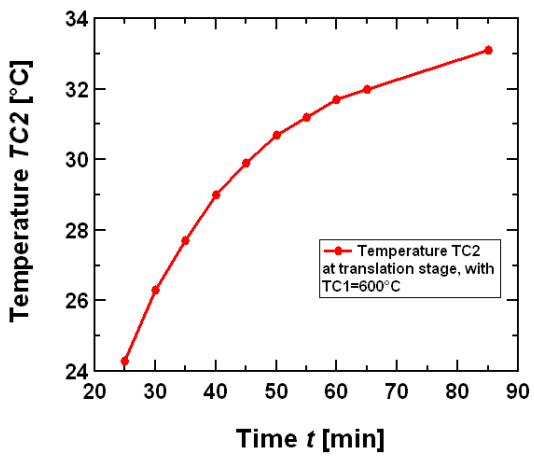

Figure 4.3: The increase of the temperature at the adapter to the translation stage after 85 minutes with a set temperature of 600°C in *Test 5.* The line between the measured points is a guide to the eye

used to block the laser light to enter the camera. This was done by replacing the plastic foil with a 8 micrometer thick Kapton®-foil coated with a 50 nm layer of aluminum. Kapton®was chosen in this case for its thermal stability up to 400°C and its good transparency for the used X-rays and aluminum for its good opacity for optical wavelengths but mainly for its very good transmission coefficient. The

x-ray transmission coefficient of the 50 nm aluminum layer is 99.9% and of the 8 µm Kapton®-foil approximately 95% for a x-ray energy of 4.51 keV [28].

Further many other delicate components of the setup such as cables close to the heater were covered generously with thick aluminum foil.

4.1.2 Mechanical Stability

Another problem when working with such high temperatures is that thermal expansion of the heater components can not be neglected (as discussed in 3.3.4) if we want to achieve high angular resolution to observe the shift of the Bragg reflection in our setup.

Therefore we implemented a system that monitors the tilt of the sample during an experiment to correct the measured X-ray data. Technically this was accomplished with a setup as sketched in Fig. 4.4. There the reflection of a HeNe-laser beam from the sample surface is detected with an CCD camera with a pixel size of 6.7 μm. From a calibration measurement where the sample was rotated in steps of 0.02° while the position of the focussed laser beam was observed a calibration factor of 0.002° $\hat{=}$ -5.7 Pixel results. The error of this factor is given by the error of the linear fit (see Fig. 4.9) which is of an order of one standard deviation ± 6 Px/deg or $\pm 0.2\%$. This measurement therefor shows that the angular tilt of the sample can be measured with an resolution of approximately $\pm 0.002°$ which is sufficient for our experiment. In Chapter 4.2.2 we will see how this system works during an experiment.

4.2 Characterization of Thin PZT Films

The measurements to be discussed in this chapter were performed using the Ti $K\alpha_1$ laser-plasma source (Chapter 3.2) with a X-ray photon energy of 4.51 keV. The samples under investigation were commercially available (PHASIS, [46]) epitaxially grown lead zirconate titanate, also $Pb(Zr_{0.2}Ti_{0.8})O_3$ or PZT, thin films on a (001)

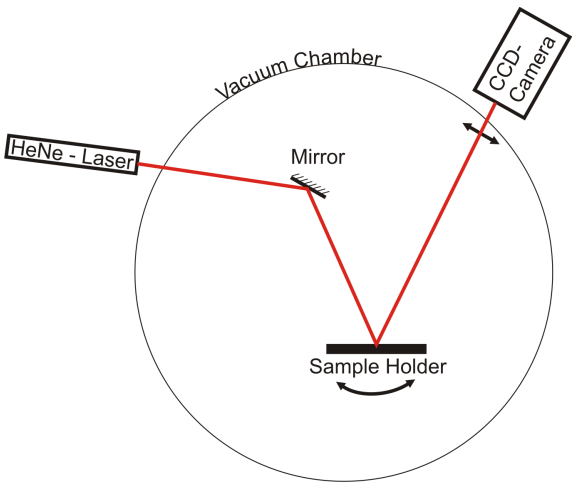

Figure 4.4: A sketch of the in-situ monitoring system of the sample tilt

strontium titanate, $SrTiO_3$ or STO, substrate using off-axis RF magnetron sputtering [37]. The samples are available either on insulating STO or on conducting 1 at% Nb-doped STO substrate [47]. The various samples are listed in table 4.2.

PZT is an alloyed perovskite with different properties according to the ratio of Zr/Ti. At room temperature $PbZrO_3$ is anti-ferroelectric and $PbTiO_3$ a tetragonal ferroelectric material [48] (see phase diagram in Fig. 4.10). A higher Ti concentration results in a higher remanent polarization and a better lattice match to the $SrTiO_3$ substrate whereas a higher concentration of Zr lowers the ferroelectric Curie-temperature T_C.

The PZT films available are grown in crystallographic (001) direction with their tetragonally distorted c-axis normal to the sample surface. As already pointed out in Chapter 2.2, the polarization of ferroelectric crystals depends on the tetragonally distortion of the unit cell, and therefore the polarization not only changes when the length of the c-axis is varied, but is also coupled to the a-axes. As a consequence, growing PZT with an a-axis of 3.9525 Å and c-axis of 4.1484 Å on (001) oriented cubic STO with an lattice parameter of 3.905 Å, leads to formation of out-of-plane, c-axis oriented domains due to the compressive epitaxial strain imposed on the film by the substrate [49, 50, 51]. In the following measurements we will observe the

Figure 4.5: Sample tilt of +0.1°.

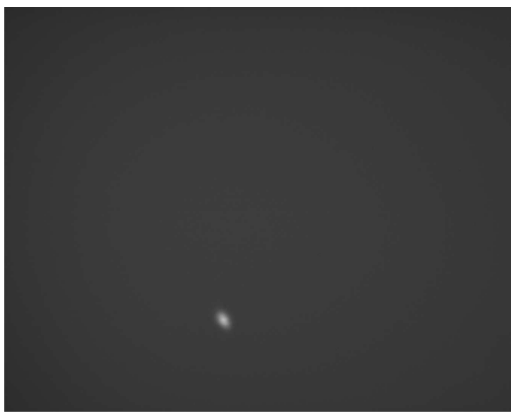

Figure 4.6: Sample tilt of +0.04°.

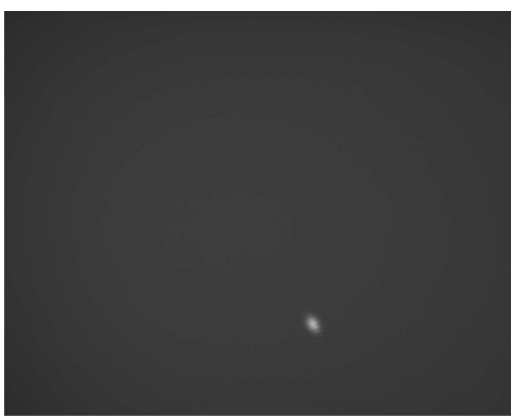

Figure 4.7: Sample tilt of -0.04°.

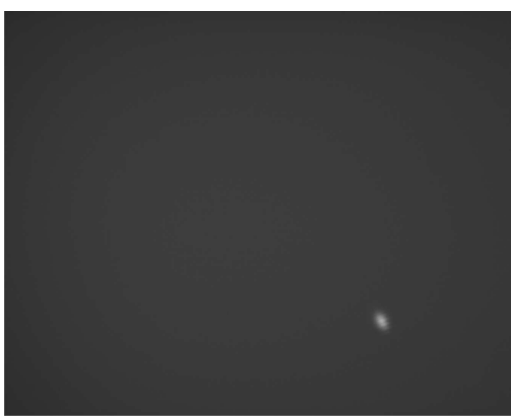

Figure 4.8: Sample tilt of -0.1°.

changes of the *c*-axis parameter as an indicator for the net polarization in the film.

The values for the lattice parameter of the *c*-axis in table 4.2 were calculated from X-ray diffraction measurements performed by PHASIS (see Fig. 4.11) for each particular sample. These diffractograms were supplied by PHASIS as printed images. The angular scale was calibrated by the position of the STO-reflection. The error of the lattice parameters extracted from those images is determined by the reading accuracy of the peak positions from the printed diffractograms. With a reading accuracy of ±1 mm the angular error equates to about ±0.009° which leads to an uncertainty of about ±0.006 Å in determining the lattice parameters from the printed images. In order to confirm the accuracy of the diffractograms the position

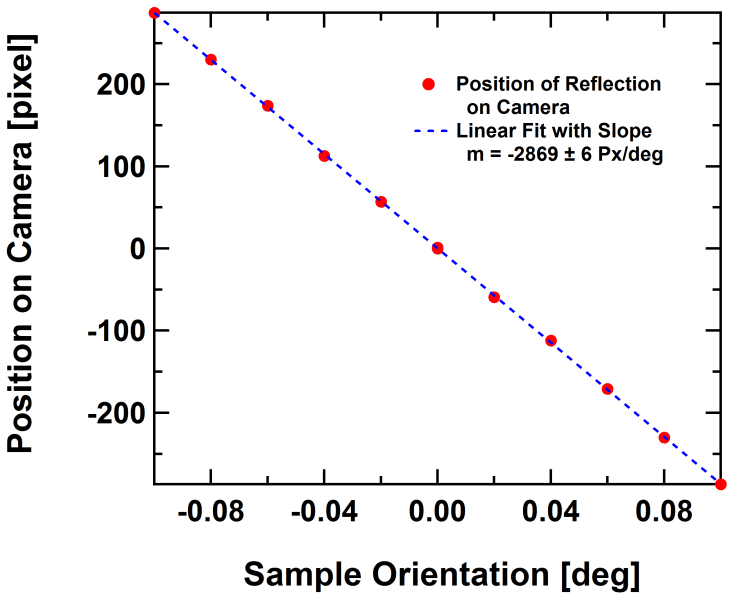

Figure 4.9: Calibration curve of the HeNe-laser monitor. X-position of the spot on the camera plotted as a function of the sample tilt. The blue dotted line is a linear fit of the measured data.

of the STO peak was measured as well and compared with the literature value of 3.905 Å and lie within the specified error.

Comparing the different samples in Table 4.2 one notices the sensitive dependence of the *c*-axis lattice parameter, and thus the polarization, on the properties of the film-substrate-system (i.e. the conductivity of the substrate and the film thickness). Even films with nominal same parameters (e.g. #P8130_100 and #P8123_100) exhibit a noticeable difference in the length of the *c*-axis.

Experimental data for the lattice parameter of the 100 nm sample #P8130_100 on Nb:STO as well as the temperature dependence will be presented in more detail in the following section.

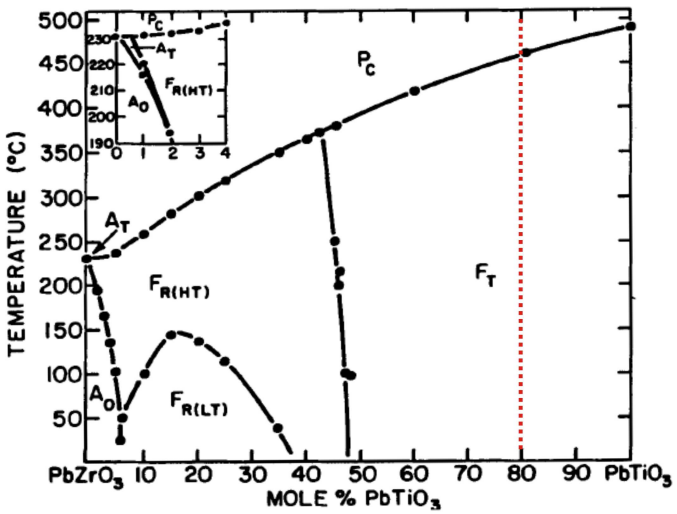

Figure 4.10: Phase diagram for different concentrations of Ti and Zr in PZT. The dashed red line marks the 20/80 composition of the PZT samples used in this experiment. F_T*:* Ferroelectric tetragonal phase, P_C*:* Paralectric cubic phase, F_R*:* Ferroelectric rhombohedral phase, A_T*:* Antiferroelectric tetragonal phase, A_O*:* Antiferroelectric orthorhombic phase *(Figure by Jaffe* et al.*[48])*

4.2.1 Sample "100 nm" PZT/Nb-STO

To test the new sample holder, one of the "100 nm" samples #P8130_100 on the conducting substrate was chosen. Using the *c*-axis lattice constant of 4.14 Å obtained from the diffractogram provided by the manufacturer (see Fig. 4.11) the Bragg-angle for the (001) reflection at 4.51 keV is calculated as $\vartheta_{PZT} = 19.39°$. For the STO-substrate $\vartheta_{STO} = 20.61°$ [52], this is only 1.2° away from the PZT-peak. Therefore, both rocking curves lie close enough together to record them simultaneously on the CCD-camera without having to actually rotate the sample (see Fig. 4.13). This is because we use a mirror to focus the X-rays on to the sample with a large convergence angle of $\approx 1.4°$ (see Chapter 3.2.2). Hence we can easily calibrate the absolute angular shift of the PZT peak to the STO peak and also compare other parameters like the shape of the rocking curve or the diffracted intensity.

Tabelle 4.2: List of $Pb(Zr_{0.2}Ti_{0.8})O_3$ thin-film samples available for investigation with their lattice parameters and type of substrate

Sample	Film Thickness, nominal	Lattice Parameter *C*-Axis PZT	Substrate
#P8130_100	100 nm	4.140 ± 0,006 Å	1.0at%Nb-$SrTiO_3$
#P8123_100	100 nm	4.128 ± 0,006 Å	1.0at%Nb-$SrTiO_3$
#P6043_80	80 nm	4.121 ± 0,006 Å	1.0at%Nb-$SrTiO_3$
#P6038_56	56 nm	4.107 ± 0,006 Å	1.0at%Nb-$SrTiO_3$
#P10046_50	50 nm	4.142 ± 0,006 Å	$SrTiO_3$

This also means that if the width and e.g. the shift of the rocking curve are smaller than the cone angle of the focused X-rays of $\approx 1.4°$ (see Chapter 3.2.2), one can record the whole rocking curve on an area detector with a single image instead of rotating the sample for every data point like in $\vartheta - 2\vartheta$ scans usually done.

Using the diffractogram of the sample provided by the manufacturer (Fig. 4.11) the true thickness of the film is determined to $d = 110 \pm 5$ nm from the spacing of the so-called thickness fringes **??**.

Diffraction Image and Rocking Curve

An important factor for carrying out experiments with the Ti-K_α setup, to achieve a good signal to noise ratio for a high accuracy of the collected data as well as a reasonable integration time of the image acquisition (e.g. 60 s - 120 s), is the strength of the diffraction signal. Measurements performed by Shymanovich *et al.* show that

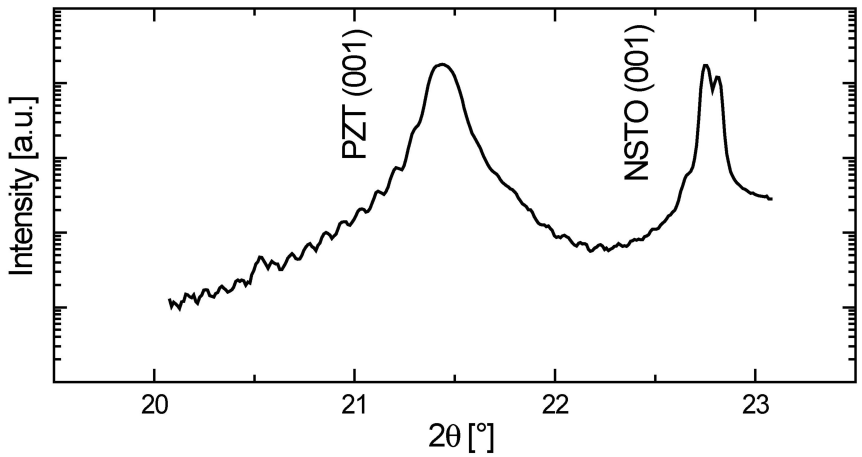

Figure 4.11: Cu-K X-ray diffraction analysis $\vartheta - 2\vartheta$ scan on the 100 nm sample #P8130_100. The fringes on the shoulders are due to reflections from the film interfaces from which the thickness of the PZT films may also be calculated. Note also the the double peak of NSTO resulting from the spectrum of the incident X-rays containing the $K\alpha_1$ and $K\alpha_2$ emission lines of Cu. The double peak for the thin PZT film is hidden by the large width of the rocking curve. Source: PHASIS [46]

approximately $5 \cdot 10^4$ photons per X-ray pulse are reflected from the toroidally bent mirror onto the sample surface. But depending on the sample typically only a few photons per pulse are diffracted and reach the X-ray detector. As an example I would like to compare the diffraction images and the rocking curves from an 100 nm iron rhodium (FeRh) thin film to that of the nominal 100 nm PZT sample as found in Fig. 4.12 through 4.15.

Comparing the diffraction images in Fig. 4.12 and 4.13 it is obvious that the (001) peaks from PZT and STO are significantly sharper and more intense than the (100) FeRh peak. Please not that both images were acquired under the same experimental circumstances i.e. the were integrated over 1200 X-ray pulses[1] of the same intensity. The rocking curves of the corresponding diffraction peaks are shown

[1]Corresponds to an integration time of 120s

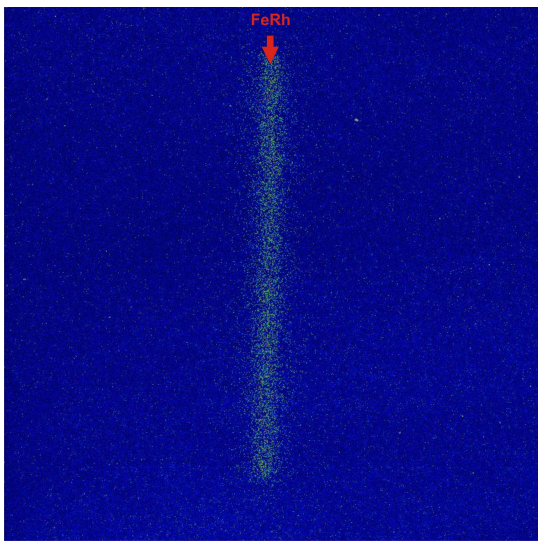

Figure 4.12: False-color camera image of the (001) diffraction peak a 100 nm FeRh film. Acquired in the Ti-K_α-setup at room temperature with an acquisition time of 120s at a repetition rate of 10 Hz. Note the much broader and weaker signal.

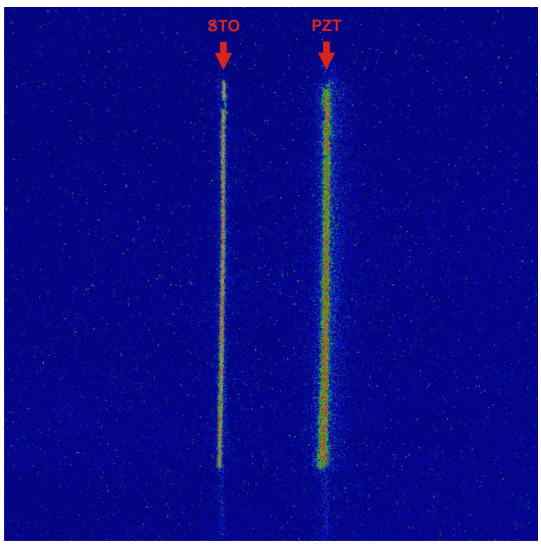

Figure 4.13: False-color camera image of the two (001) diffraction peaks of bulk STO and the 100 nm PZT film. Acquired in the Ti-K_α-setup at room temperature with an acquisition time of 120s at a repetition rate of 10 Hz. Note the sharp diffraction signals compared to the FeRh films of same thickness and same exposure time.

in Fig. 4.14 and 4.15. The rocking curves are obtained by integrating vertically over the diffraction signal. The measured full width at half maximum (FWHM) of the FeRh rocking curve is 0.244° and for the measured rocking curve of PZT the FWHM is 0.09°. The focal spot size of the X-ray beam on the sample (approx. 90µm) limits the angular resolution to approximately 0.04°. Thereby the size of the X-ray focus isn't a dominant factor for the broadening of the rocking curves of the thin films but is the limiting factor for the STO-peak which has a measured FWHM of approx. 0.04° (not shown here).

Due to the mosaic structure of the film, the FeRh-diffraction peak is also significantly wider than what is expected for a perfect 100 nm thick film (0.079°). Measurements by Quirin on the nominal '100 nm' FeRh film yield a thickness of

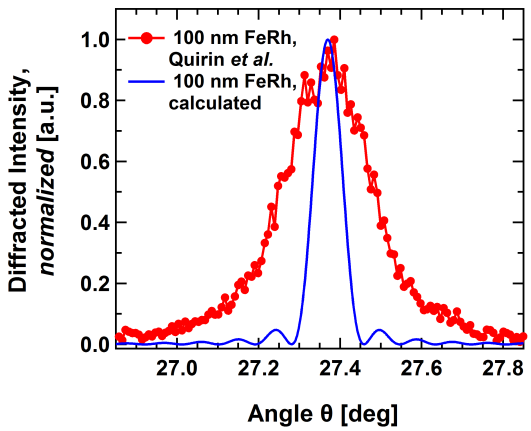

Figure 4.14: Rocking curve of the diffraction peak in Fig. 4.12 (red dots; the continuous red line is a guide to the eye). For comparison the theoretically calculated rocking curve (blue line) by XOP [3]. See work by Quirin *et al. [32, 33].*

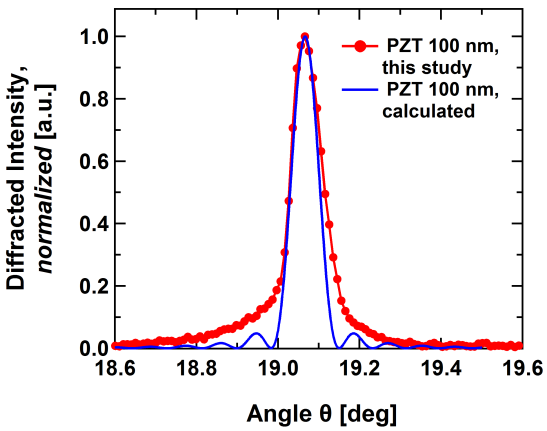

Figure 4.15: Rocking curve of the PZT peak in Fig. 4.13 (red dots and line). For comparison the theoretical calculated rocking curve by XOP [3] is also shown (blue line).

approximately 93 - 96 nm [33]. The measured width of the PZT-diffraction peak is almost equal to the width for a perfect film (see blue curve in Fig. 4.15) evidencing the good crystalline quality of the film. However, it should be noted that the measured rocking curve does not show the expected thickness fringes in the diffraction signal [4]. Instead the measured rocking curve exhibits pronounced wings. Such a behavior has been reported by Gariglio *et al.* **??** and is attributed to misfit dislocations which relax the stress in thick films due to the in-plane lattice mismatch between film and the substrate. The disorder introduced by the dislocations and the corresponding gradient in the lattice parameter causes the broad background/wings in the diffraction signal.

As one can calculate from the integrated reflectivity of the rocking curve about 5 - 7 photons per pulse are scattered from the FeRh sample (see measurements by Quirin [33]) whereas the PZT sample scatters about 23 Photons per pulse. The difference can be attributed to the the atomic scattering factor discussed in Chapter

2.1.1 which depends on the atomic number Z and the distribution of the electrons in the atoms. Since lead with an atomic number of 82 is the main component of PZT a larger diffraction efficiency as compared to FeRh (atomic numbers 26 and 45) is expected. Comparison with XOP-calculations support this view, although they predict a somewhat smaller ratio of about 2.5 between the PZT and FeRh diffraction efficiency.

4.2.2 Temperature Dependence of Lattice Constant

To further characterize the 100 nm PZT sample on conducting Nb:STO substrate measurements were carried out to determine the temperature dependence of the c-axis lattice parameter of PZT. Starting at room temperature the sample was first heated in steps of 50°C close to T_C where the structural phase transition - ferroelectric to paralectric - occurs and then in steps of 10°C up to a temperature of 810°C. Sufficient thermal stability was provided by the temperature controller to an accuracy of better than 1%. According to Gariglio *et al.* ([37] and references mentioned there) the transition temperature for thin films lies around 680°C, a much higher value than for the bulk material which is about 470°C [36]. This is attributed to the strain from the 2-dimensional clamping of the film to the slightly different lattice constant of the substrate. It is worth noting at this point that Paruch *et al.* report the transition temperature $T_C \approx 785$°C in 50 nm and 91 nm $Pb(Zr_{0.2}Ti_{0.8})O_3$ films on Nb:STO. They directly measured temperature at which the domains have disappeared [45].

The results shown in Fig. 4.17 and Fig. 4.18 are already corrected with the angular correction data acquired with the HeNe-monitoring setup plotted in Fig. 4.16. What we see in these measurements is that the shift of the Bragg-angle of PZT qualitatively behaves as shown by Janolin *et al.* for 100 nm PZT of the same composition on isolating STO, but differs significantly from data obtained by Gariglio *et al.* for 40 nm PZT of the same composition on conducting Nb:STO [Fig.

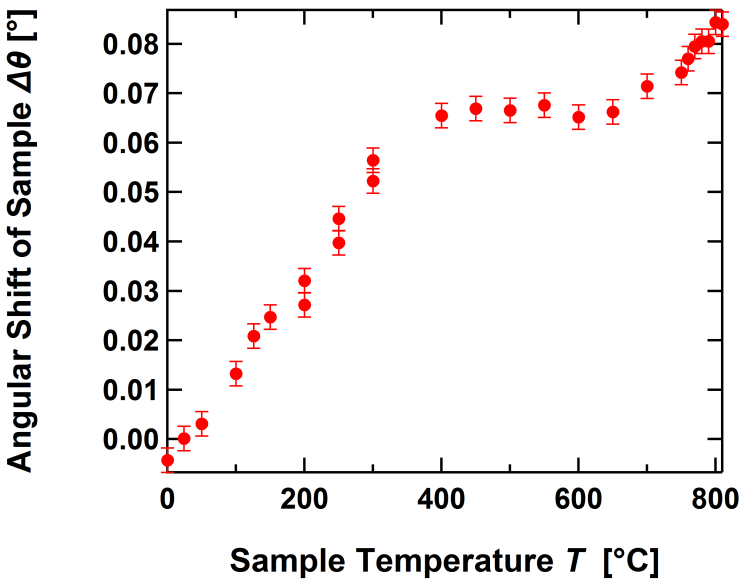

Figure 4.16: Angular tilt in $\Delta\vartheta$ of the sample holder as a function of the sample temperature. Monitored during the experiment by observing the shift of the HeNe-laser reflection.

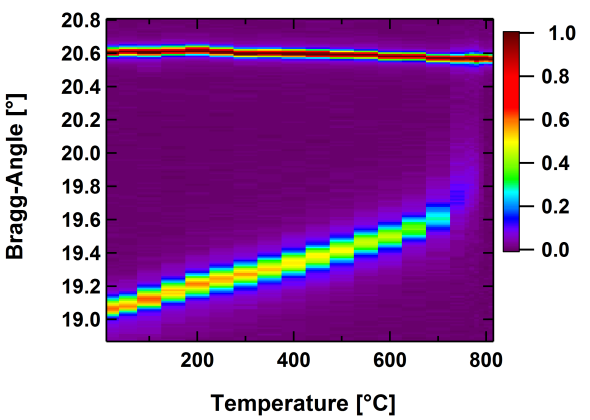

Figure 4.17: Color coded Image of the temperature dependence of the Bragg angle of PZT on Nb:STO corrected by the data from the HeNe-monitor. The diffracted intensity is coded by the color scale.

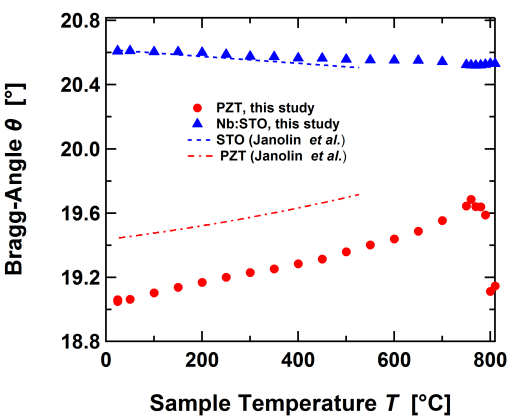

Figure 4.18: Shift of the center of mass of PZT and Nb:STO compared to results obtained by Janolin *et al* [53]

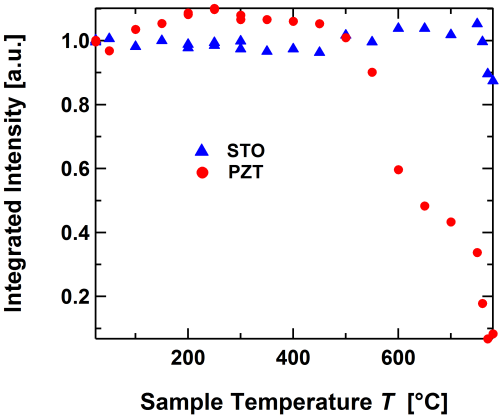

Figure 4.19: Integrated intensity of the PZT and STO reflection as a function of temperature normalized to the incident X-ray photons and the intensity at room temperature

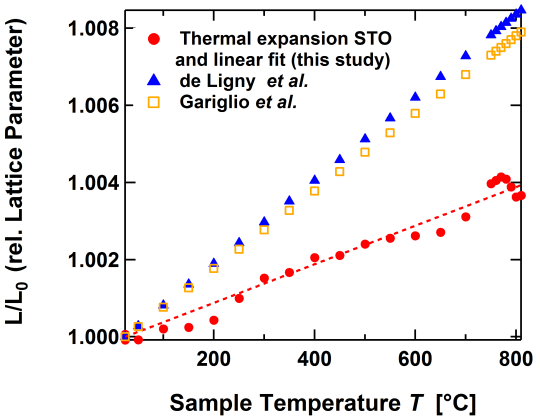

Figure 4.20: Comparison of the measured thermal expansion of STO (red dots) to the literature value investigated by de Ligny *et al.* [54] (blue triangles) and Gariglio *et al.* [37](orange squares)

4.21 (a)]. For temperatures smaller than approximately 600°C the shift changes nearly linear with temperature. Then for temperatures higher than 600°C when we get closer to the transition temperature T_C the lattice parameter for the c-axis decreases more rapidly until it reaches its minimum around 750°C. After this point PZT enters the paralectric phase. Due to the strain imposed on the a-axis by the substrate, the PZT unit cell does not enter the cubic phase but remains tetragonally distorted. For a cubic phase the PZT peak would merge into the substrate but due to the constraint the substrate imposes on the a-axes, the paraelectric phase must not necessarily be cubic. The blue dots in Fig. 4.21 (a) of Gariglio *et al.* show the a-axis of PZT following the thermal expansion of the Nb:STO substrate. As one can see in Fig. 4.22 the shift to smaller angles above 780°C is rather attributed to the vanishing signal of the PZT peak than to a real shift.

One can also see clearly in Fig. 4.19, Fig. 4.22 and in the false-color image Fig. 4.17 as well, the dramatic drop in intensity of the PZT reflection decreasing drastically at 750°C until it completely vanishes reaching about 790°C - 800°C.

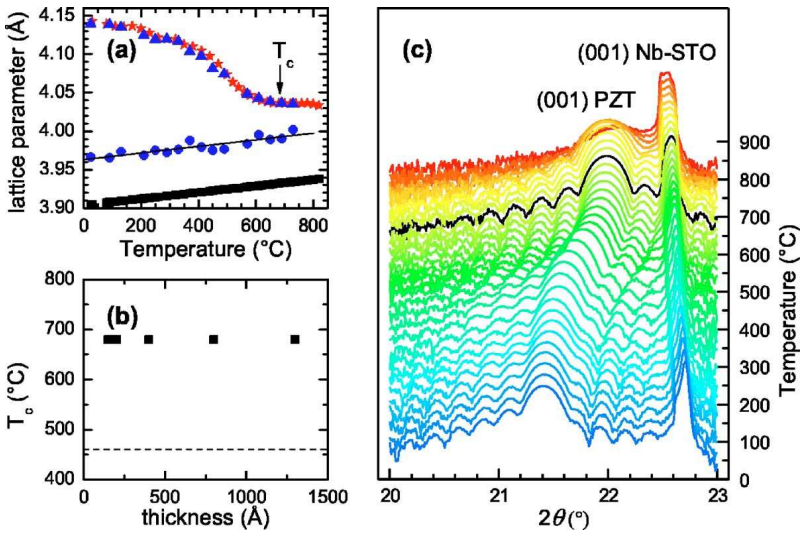

Figure 4.21: (a) Measurements by Gariglio *et al.* showing the change of the *c*-axis lattice parameter of 40 nm $Pb(Zr_{0.2}Ti_{0.8})O_3$ (blue triangles) from(103)-reflection, the (001)-reflection (red stars), the *a*-axis parameter (blue dots) and the lattice parameter for the Nb:$SrTiO_3$ substrate (black squares) with temperature. T_C is around 680°C [37]. (b) Phase transition temperatures vs. thickness for different PZT thin films. (c) Intensity of $\vartheta - 2\vartheta$ scans around the (001) PZT reflection as a function of temperature for the 40 nm thick film.

The complete disappearance of the PZT reflection, i.e. the drop of the intensity in Fig. 4.19 to zero at high temperatures, means nothing less than the destruction of the PZT film. This has been verified by measurement after the sample was cooled down again. The complementary slight increase of intensity of the STO reflection might also indicate the disappearance of the PZT film. From this occurrence and from the deviation of the measured thermal expansion coefficient of STO ($\approx 0.5 \cdot 10^{-5}\mathrm{K}^{-1} \pm 1.01 \cdot 10^{-7}$) to literature values ($4.1 \cdot 10^{-5}\mathrm{K}^{-1}$ de Ligny *et al.* [54], $1.01 \cdot 10^{-5}$ Gariglio *et al.*) we suppose that the temperature at the sample might not be the same as where the thermocouple is placed. For the expected transition temperature of 680°C this would mean that the sample is about 100°C colder than what TC1 shows. The thermal expansion of STO as shown in Fig. 4.20, which is

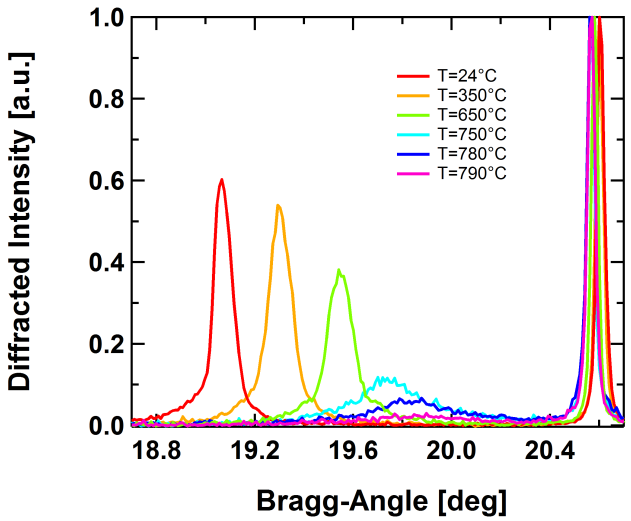

Figure 4.22: Rocking curves for 100nm PZT (left) and STO (right) and their Bragg-angle ϑ as a function of temperature.

about half the value compared to results of Gariglio *et al.* and about 10-times less than what de Ligny *et al.* claim, also points to this assumption. On the other hand, the fact that the thin film seems to have evaporated gives reason to believe that the sample was actually hotter than what TC1 indicated.

4.2.3 Conclusion

The measurements presented in Section 4.1 of this chapter show that the heater is able to reach the temperatures required to drive the PZT sample into the paraelectric phase and can be operated safely with the measures taken to prevent thermal damage to the components in the setup. Also it has been shown that the thermal expansion of the heater is under control by in-situ monitoring of the tilt of the sample with the HeNe-laser reflection. The obtained data on the sample tilt can be used to correct the measured shift of the diffraction signal to an accuracy of $\pm 0.002°$.

What remains is the question if the temperature measured by TC1 reflects the

actual temperature of the sample (see Section 4.2.2).

We have also shown in Section 4.2 that the diffraction signal from the PZT thin film is sufficiently strong to carry out experiments with the Ti$K\alpha$-setup. Characterization of the sample by observing the change of the c-axis parameter as function of temperature has revealed that the qualitative behavior is in accordance with measurements by de Ligny *et al.* but show significant departures compared to the results of Gariglio *et al.*. Effects due to screening of the polarization by surface adsorbates or free charges [55] and interface/surface defects by oxygen vacancies and dislocations [53] still have to be investigated.

The destruction of the sample at high temperatures is a serious problem that must be carefully examined. The measurements by Gariglio *et al.* [37] were done up to 900°C in air and no such problems were reported. It is possible that the absence of air/oxygen in the evacuated experimental chamber might lead to diffusion processes of the oxygen and therefore lead to destruction of the crystalline structure of the sample. It should also be noted that Paruch *et al.* report a significant increase of the surface roughness from 0.4 - 0.5 nm root-mean-square (rms) at room temperature to 7.1 nm rms after heating to 785°C and further deterioration of the sample surface to a roughness of 15.1 nm rms after heating to 885°C [45].

Further careful experiments where e.g. the temperature is measured directly at the sample, heating the sample at atmospheric pressure and Atomic Force Microscopy (AFM) measurements of the sample surface might help to provide more information for determining the exact reason for these apparent contradictions.

4.3 Optical Manipulation of Polarization in Thin PTO Films

Experiments presented in this chapter was on similar thin films to those described above and will be described in more detail in Section 4.3.2 of this chapter. The experiments were performed at the X-ray pump-probe (XPP) experimental station at the LCLS (Linac Coherent Light Source) at SLAC in Menlo Park, USA (see also 3.1). The LCLS is the first X-ray Free Electron Laser (FEL) to produce light pulses in the hard X-ray regime down to a wavelength of 0.12 nm and pulse durations from 500 fs down to less than 10 fs with full spatial coherence [11] with pulse energies of up to 3 mJ which means about 10^{12} photons per pulse one can even carry out single pulse experiments which wouldn't be possible at X-ray sources such as the laser-plasma source at the University Duisburg-Essen (UDE). There it is necessary to integrate over as many as e.g. 1200 pulses in the case of FeRh or PZT to get a good signal to noise ratio.

First analysis of time resolved X-ray diffraction studies with sub-picosecond time resolution in metal/ferroelectric/metal ($SrRuO_3$/PZT/$SrRuO_3$) nanolayer systems have been reported by Korff Schmising *et al.* Subject to investigation were polarization and lattice dynamics after ultra-fast laser excitation of the metallic $SrRuO_3$ nanolayers in the superlattice. This produces high stress in the $SrRuO_3$ layers compressing the PZT nanolayers, leading to an expansion of the entire superlattice in approximately 30ps [56].

Other works, for example of Li *et al.* , report ultra-fast polarization switching in fully integrated Pt/$(La_{0.5}Sr_{0.5})CoO_3$/ $Pb(Nb_{0.04}Zr_{0.28}Ti_{0.68})O_3$ /$(La_{0.5}Sr_{0.5})CoO_3$/Pt capacitors switched by sub-100 ps rise step-function-like electrical pulses.

Here in this section studies are presented, where polarization changes in lead titanate ($PbTiO_3$, PTO) thin films are directly manipulated by laser excitation

without the use of intermediary electrodes.

4.3.1 Experimental Parameters at the LCLS

The aim of the following experiments was to perform time resolved optical pump - X-ray probe measurements at different temperatures (Room temperature, just below T_C and just above T_C) in a $\vartheta - \vartheta$ [is this correct?] X-ray diffraction configuration using a large area X-ray photodiode as a detector. The delivered X-ray beam was monochromatized using a Si (111) double-crystal monochromator leaving $\approx 10^{10}$ photons per pulse reaching the sample.

Table 4.3 shows the significant FEL beam parameters for the following experiment.

Tabelle 4.3: Experimental Parameters of the delivered FEL-beam

Parameter	Value
FEL Energy	9000 eV
Electron Bunch Charge	150 pC
Repitition Rate	60 Hz
Pulse Energy	1.13 mJ
Photons per pulse	$8 \cdot 10^{11}$ Photons
Pulse duration	$\approx$ 60 fs

For optical excitation we used ultrashort laser pulses with a FWHM duration of 40 fs at a wavelength of 400nm because ellipsometrical measurements done by Daranciang, Lindenberg *et al.* [57] to determine the optical constants of PTO show that (Fig. 4.23) PTO is nearly transparent for 800 nm wavelength . Therefor the 800 nm pulses of a Ti:sapphire laser were frequency-doubled in an BBO crystal (see Chapter about 800/400nm pump branch) by SHG to a maximum incident fluence of 5 mJ/cm^2.

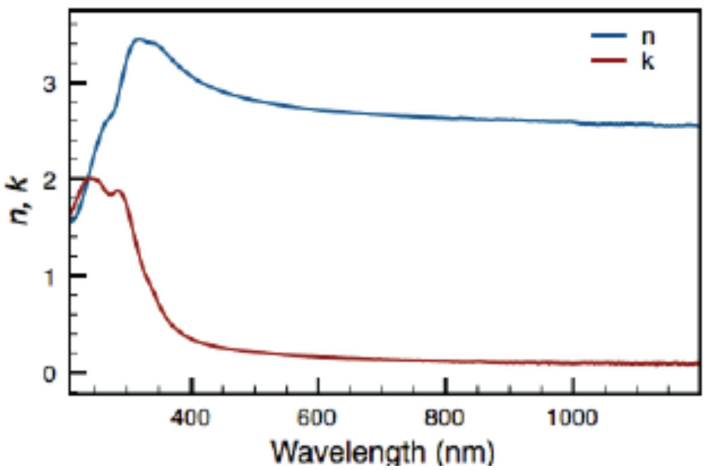

Figure 4.23: Ellipsometrical measurements to determine the optical constants of 20 nm PTO deposited on STO (001). Lindenberg *et al.* *[57]*

The s-polarized 400 nm optical pump beam was nearly collinear with the X-ray beam and could be delayed relatively to the X-ray pulses with a motorized delay stage. The spot size of the X-ray beam was about 500 μm x 1000 µm and 1.5 mm x 3 mm of the optical beam. By choosing the focal spot pump beam more than twice the size of the probe beam the lateral excitation can be assumed almost homogeneous. The sample was mounted on a water cooled heater on a calibrated high precision goniometer shown in Fig. 3.8.

4.3.2 Ferroelectric Samples and Measurements

The aims of the experiments presented in this section were to investigate the transient response and the polarization dynamics in ferroelectric PTO thin films after laser excitation with a time-resolution $<$ 100 fs. Therefore we observed the change of the *c*-axis lattice parameter, which is directly coupled to the polarization of the film. An increase of the *c*-axis lattice parameter increases the polarization and a decrease of the *c*-axis a decrease of the polarization. We can directly investigate the evolution of the polarization by measuring the shift of the diffraction signal, the

diffracted intensity and the shape of the rocking curves as a function of laser delay and temperature for different PTO thin film-systems.

The first sample presented in this study is a (001) oriented 20 nm PTO film epitaxially grown via metal-organic vapor deposition on [non-conducting!] (001) STO substrate. Ramana Murty *et al.* give a description of the manufacturing procedure [58]. As mentioned earlier in Section 4.2, PZT grown on (001) STO forms out-of-plane, *c*-axis oriented domains below the ferroelectric Curie-temperature $T_C = 680°C$ [37] due to the lattice mismatch to the STO substrate.

For this sample measurements were performed at room temperature, where the thin film is in its ferroelectric mono-domain, and at 515°C where the film is in its ferroelectric stripe phase. Minimization of the energy of the electric field caused by the polarization leads to the formation of 180° stripe domains which are periodic, lamellar regions of alternating polarization. The thickness-dependent periodicity for this 20 nm film is of the order of 10 nm (see also Chapter 2.2 and [49]).

The second sample under investigation was also a PTO thin film but grown on a different substrate. To get a better lattice match between the PTO thin film and the substrate, films have been grown on (110) oriented dysprosium scandate ($DyScO_3$, DSO) [59]. In this orientation DSO has a near square surface with an in-plane lattice constant of $a_{DSO} = 3.944$ Åcompared to a_{PTO}=3.9525 Å for PTO and $a_{STO} = 3.905$ Å for (001) oriented STO (see also Section 4.2). This makes it possible to heat the sample statically above T_C, which meets approximately 470°C for this sample [36], into or very close to its cubic, paraelectric phase. Other than on the STO substrate, where the lattice mismatch forces the film to grow with its tetragonally distorted *c*-axis out-of-plane [53], the near-lattice match on the (110) DSO substrate also allows PTO to grow with its *c*-axis in-plane.

The thickness of the PTO film was declared to be a '100 nm' film but as we will see from the thickness fringes of the rocking curves recorded in this measurement

(Fig. 4.37) the the nominal thickness must be approximately 300 nm (Calculation see Section **??**).

The measurements on the 300 nm PTO/DSO thin film were carried out at different temperatures relative to T_C: far below (room temperature), below (430°C) and above (450°C). Obviously, 450°C isn't the nominal Curie-temperature but we will see later in Section 4.3.6 by the shape and the behavior of the rocking curves that the actual temperature of the sample is higher than the nominal temperature.

4.3.3 Sample 20 nm PTO/STO - at Room Temperature

Fig. 4.24 and 4.25 show the rocking curves of the (003) reflection at different times after laser excitation with a fluence of 5 mJ/cm^2 taken at room temperature where PTO is in tetragonal ferroelectric phase. The Bragg-angle of the (003)-reflection in this film lies at $\vartheta = 29.85°$.

The side-peaks, or so-called thickness fringes visible in the rocking curves in Fig. 4.24 show the good crystalline quality, i.e. that there is no or little mosaic spread in the film causing additional broadening of the curve. The continuous line connecting results from fitting the curves with a multi-peak Voigt[2] fit. Table 4.4 shows some parameters gained from the fit-parameters of the rocking curves in Fig. 4.24. Comparing the full widths at half maximum (FWHM) and the integrated intensities show that the shapes of the curves for the different time delays remain nearly unchanged. This indicates that the compression and expansion of the film is homogeneous.

The symmetric shift of the rocking curves to higher angles after approx. 5 ps is followed by a shift to lower angles after 15 ps. This behavior indicates first compression along the c-axis and a reduction of the polarization. Then the after $\approx=$ 15 ps an expansion along the c-axis is observed, indicating an induced increase

[2] A Voigt profile results from the convolution of a Gaussian profile and a Lorentz profile.

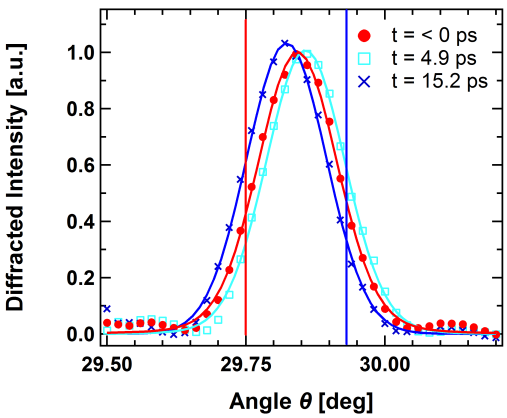

Figure 4.24: Rocking curves of PTO on STO at room temperature for different time delays after laser excitation. The measured data points were fitted with a Voigt-fit. The vertical red and blue line mark the positions $\vartheta = 29.75°$ and $\vartheta = 29.93°$, respectively, where the time-scans of Fig. **??** were taken.

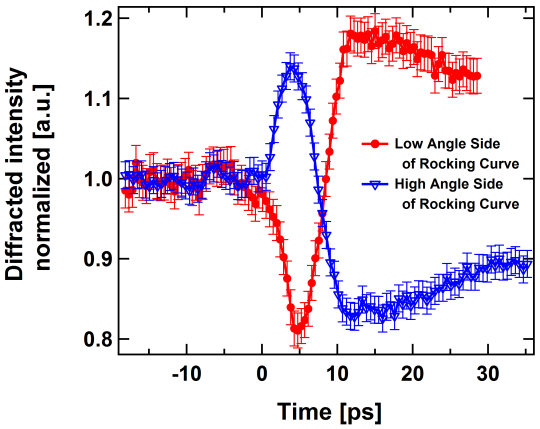

Figure 4.25: 20 nm PTO/STO, room temperature: Shift of the of the (003) reflection corresponding to the transient lattice response measured on the low-angle (red dots) $\vartheta = 29.75°$ and the high-angle side (blue triangles) $\vartheta = 29.93°$ of the rocking curves in Fig. **??**

Tabelle 4.4: FWHM and integrated intensities of the rocking curves from Fig. 4.24

Time Delay	FWHM	Integrated Intensity [a.u.]
0 ps	0.01674°	1.0000
4.9 ps	0.01672°	0.9841
15.2 ps	0.01682°	0.9802

of polarization.

To scan the transient behavior of the lattice dynamics using a collimated beam the sample is rotated to a certain position ϑ of the rocking curve (e.g. on the slope of half maximum, or at the peak position) and then the time-scan is done for that

position on the rocking curve. Using a collimated beam as done at the LCLS, this is the only way and rather than measuring the true shift of a X-ray reflection one measures the change of intensity at the chosen point on the rocking curve. In the case shown in Fig. 4.24 the shape of the rocking barely changes after laser excitation. Therefore one can interpret the intensity change at the positions marked in Fig. 4.24 as shifts of the diffraction peak.

Comparing the two time-scans on each side of the rocking curves in Fig. 4.25 we first see compression of the c-axis indicated by a shift of the rocking curve to higher angles until its minimum is reached about 5 ps after laser excitation. Then the peak starts sloshing to lower angles on a similar time-scale, indicating an elongation of the c-axis . This shift to lower angles holds on until it reached its maximum approximately 12 ps after excitation and remains at lower angles on a longer time scale. This behavior can be interpreted as a decrease in polarization for the first 5 ps which is followed ba a long-lived polarization enhancement.

If one calculates the time-of-travel t_{ac} of an acoustic wave generated by the instant excitation of the film with thickness d_{film} with the laser pulse (see Chapter **??** about effects of optical excitation and [30, 27]) assuming a sound-velocity of approximately 4500 m/s [56, 60] on gets

$$\frac{d_{film}}{v_{sound}} = t_{ac} \tag{4.1}$$

$$\rightarrow \quad \frac{20\,\mathrm{nm}}{4500\frac{\mathrm{m}}{\mathrm{s}}} \approx 4.4\mathrm{ps}. \tag{4.2}$$

The time $t_{ac} \approx 4.4$ ps computed in equation 4.2 is in good agreement with the time scale of the initial shift of the rocking curve in Fig. 4.24 and 4.25. Hence, the initial decrease in polarization is limited by the sound-velocity in the crystal.

4.3.4 Sample 20 nm PTO/STO - at 515°C (Stripe Phase)

As discussed in Section 4.3.2 of this Chapter and in Chapter 2.2, ferroelectric materials form domains similar to those observed in ferromagnetic materials in order to minimize the external electric field. The formation of 180° stripe domains, a periodic arrangement of lamella with alternating sign in polarization form out as a function of film thickness and temperature [49, 61]. Fig. 4.26 schematically shows a cross-section of a thin PTO film on STO in its monodomain phase. The polarization **P**, symbolized by arrows is oriented in one direction over the entire film. A schematic cross-section of a PTO film in its 180° stripe phase is shown in Fig. 4.27. The orientation of the polarization **P** alternates periodically along the cross-section. For the thin film of 20 nm used here, the period of the stripe domains changes from nearly monodomain structure at room temperature to a period of ≈ 10 nm at a temperature of 515°C. The scale of 10 nm results from the explicit experimental conditions - in this case defined by the temperature, the film thickness and the properties of the substrate.

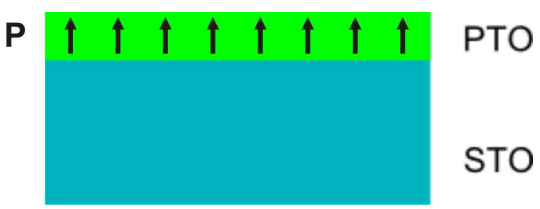

Figure 4.26: Schematic cross-section of the PTO on STO samples in a monodomain phase as present at room temperature. The arrows show the direction of the polarization ***P***.

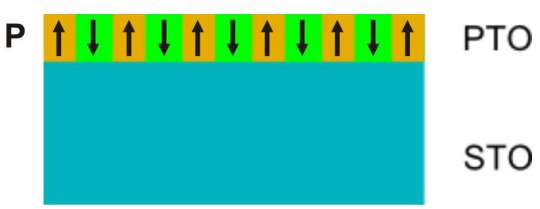

Figure 4.27: Schematic cross-section of the sample that has entered the 180° stripe phase with periodically alternating direction of the polarization ***P***.

Fig. 4.28 shows a rocking curve of the (003) reflection of the 20 nm PTO film on STO at a temperature of 515°C. At this temperature the film has already entered the stripe phase. Compared to the FWHM of the rocking curve at room temperature in the monodomain phase $\Delta_{FWHM,Mono} = 0.01674°$ the width has increased more

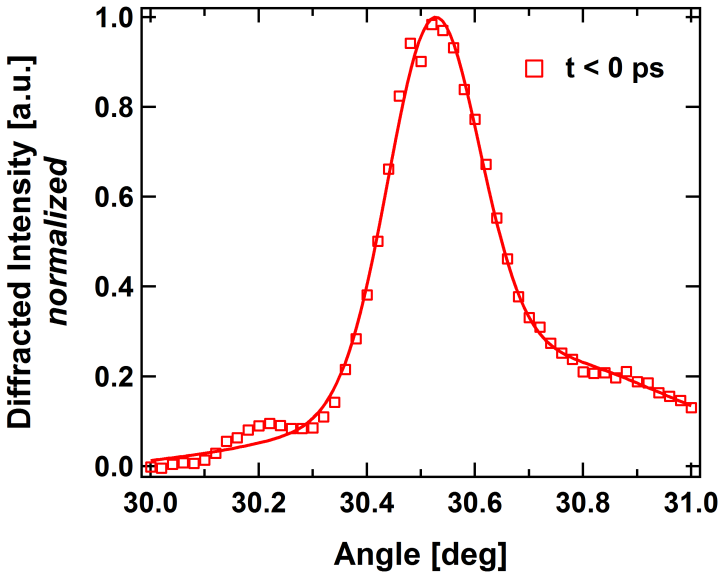

Figure 4.28: (003) Rocking curve of PTO on STO at room temperature. The continuous line connecting data points was gained by applying a multi-peak Voigt-fit.

than an order of magnitude to a value of $\Delta_{FWHM,Stripe} = 0.2302°$ for the stripe domain phase at 515°C. Additionally, the rocking curve in the stripe domain phase has become clearly asymmetric demonstrating the increased disorder in the film in due to the large number of domain walls in the stripe phase. Responsible therefore is the space of undefined polarization orientation within the domain walls where the polarization is gradually switched about 180°.

Fig. 4.29 shows the rocking curve of the PTO film without laser excitation compared to the rocking curve 33.35 ps after laser-excitation with a fluence of 5 mJ/cm^2. The FWHM of the transient rocking curve has decreased about 2.5% to $\Delta_{FWHM,Stripe} = 0.2246°$ compared to $\Delta_{FWHM,Stripe} = 0.2302°$ at $t < 0$. The high-angle shoulder of the rocking curve at t=33.35 ps has slightly increased and the diffraction intensity has decreased by approximately 1.2% showing higher degree of disorder due to the stripe domain walls.

The time-scan in Fig. 4.30 was recorded at the low-angle side, thus a shift of the rocking curve to lower angles causes the signal of the time-scan to rise meaning

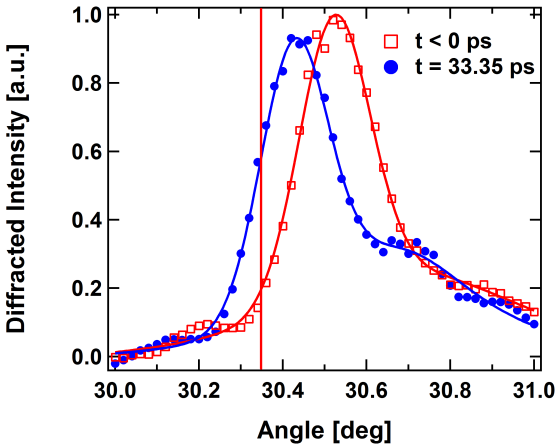

Figure 4.29: (003) Rocking curves of PTO on STO in the stripe phase at 515°C before laser excitation (red squares) and 33.35 ps after laser excitation (blue dots). The vertical red line at $\vartheta = 30.35°$ marks where the time-scan in Fig. 4.30 was measured. The continuous lines connecting data points were gained by applying a multi-peak Voigt-fit.

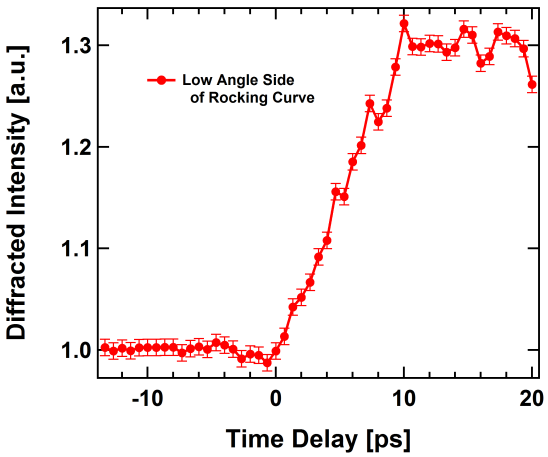

Figure 4.30: 20 nm PTO/STO @ 515°C: Time-scan on the low-angle side of the rocking curve in Fig. 4.29 at 30.35° also shows induced polarization enhancement for longer times but lacks the initial decrease in polarization as at room temperature

that the c-axis of PTO is elongated. The maximum shift is reached after a time of approximately 12 ps and exhibits a change of 30% . Comparing this transient behavior in the stripe phase to the behavior in the monodomain phase at room temperature (Fig. 4.31) shows a very similar, but stronger effect on the same time scale and without the articulated initial shift to higher angles. Close examination of the time-scans actually manifests a small shift to higher angles at times apparently before $t = 0$. It is worth noting in this context that problems concerning the temporal overlap between the pump and probe beam occurred during the experiment, in particular between the two time-scans discussed at this point. Therefore, the time-zero for the scan in the stripe phase was adjusted to fit the maximum shift to lower angles. Obviously this is in good accordance with the qualitative behavior

but the similar shifts to higher angles between $t \approx -4$ ps and $t \approx 0$ ps give rise to believe that is not quite right. Due to the uncertainties if the initial drop before $t = 0$ ps is real and in order not to manipulate the measured data this was not further corrected.

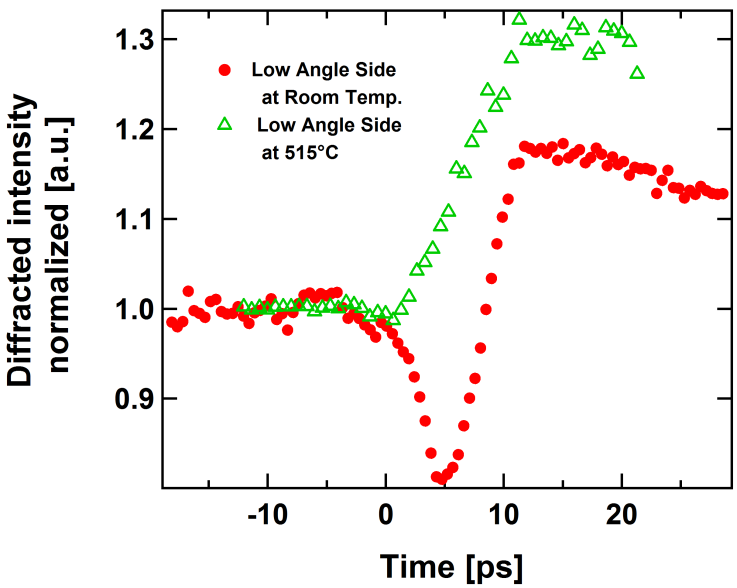

Figure 4.31: Comparison of the time-scans on the transient shift of the rocking curves in the monodomain phase at room temperature (red dots) (see also Fig. 4.25) and the stripe domain phase at 515°C (green squares). For the sake of clarity the error bars are left out.

The transient shift of the rocking curve to lower angles is equivalent to an elongation of the c-axis parameter of the PTO crystal which is equivalent to a laser-induced polarization enhancement. The effect at 515°C shows a similar, but much stronger ($\approx 67\%$) enhancement as at room temperature (Fig. 4.25) with a long-lived polarization enhancement approx. 12 ps after laser excitation with 5 mJ/cm^2. However, no or only slight decrease of polarization on the short time-scale can be observed in the stripe phase compared to the drastic decrease in the mono domain phase.

4.3.5 Sample 300 nm PTO/DSO, Ferroelectric Phase

Sample at Room temperature

Fig. 4.32 shows rocking curves of the (003) reflection of a 300 nm PTO thin film grown on (110) DSO recorded at room temperature. The curve with the red dots is before laser excitation and the curve with the blue squares is 13.4 ps after excitation. The FWHM of the curves are 0.3522° and 0.3606°, respectively. This is significantly broader compared to the rocking curves of PTO on STO in the mono domain phase at room temperature (FWHM = 0.01674°) and the stripe domain phase at 515°C (FWHM = 0.2302°) despite the much thicker film. As already mentioned at the beginning of section 4.3.2, PTO grown on (110) DSO does not only form domains with out-of-plane $c-$axis components as PTO on STO, but also with its c-axis in-plane due to the better lattice match. This results in a higher disorder in the lattice and therefore to a broader rocking curve (only the $c-$-axis contributes to the (003) rocking curve at this angle). The offset of the curve at high angles is due to the nearby substrate peak at $\vartheta = 31,5°$.

Rocking curve after laser excitation, blue squares in Fig. 4.32, show only very little effect after laser excitation with a pump fluence of 5 mJ/cm^2. The angular shift of the curve after 13.4 ps to higher angles is 0.013° and only manifests very little decrease in intensity.

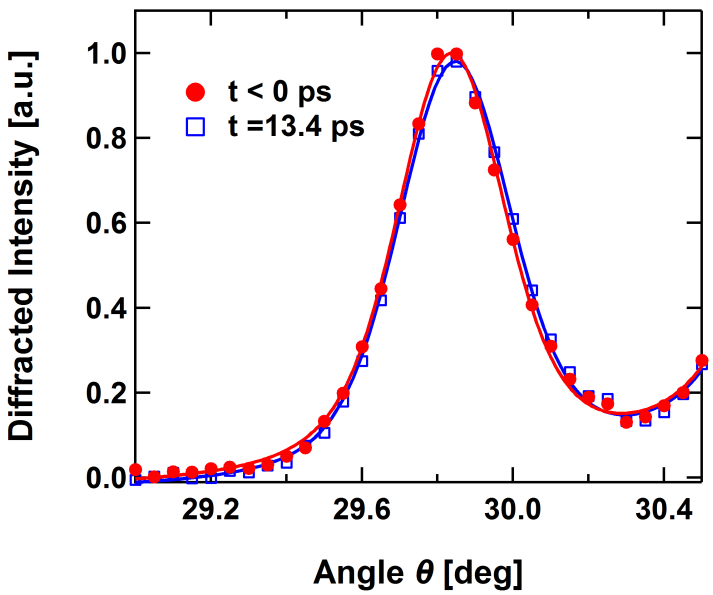

Figure 4.32: Rocking curve for the (003) PTO reflection on DSO at room temperature. Before laser excitation (red dots) and 13.4 ps (blue squares) after excitation with 5mJ/cm^2.

Sample at 430°C

After heating up the sample to a temperature of 430°C, which lies close to the Curie temperature, the magnitude of the transient effects increases significantly compared to measurements at room temperature. Actually the same (although with less amplitude) happens for the film on STO: Larger effects are observed for higher starting temperature. Figure 4.33 and 4.34 show series of rocking curves at various time delays after laser excitation with 5 mJ/cm^2.

Shortly after excitation the rocking curve starts shifting towards the substrate peak. After 90 -150 ps they merge almost completely with each other while the intensity of the DSO reflection increases at the expense of the PTO reflection. This can be seen in Fig. 4.35 which shows the integrated intensity of both, the PTO and DSO curves, normalized to the intensity before laser excitation.

Fig. 4.36 shows a time-scan recorded on the low-angle side of the rocking curves in Fig. 4.33. The shift of the curve to higher anngles depicts a drop in intesity of

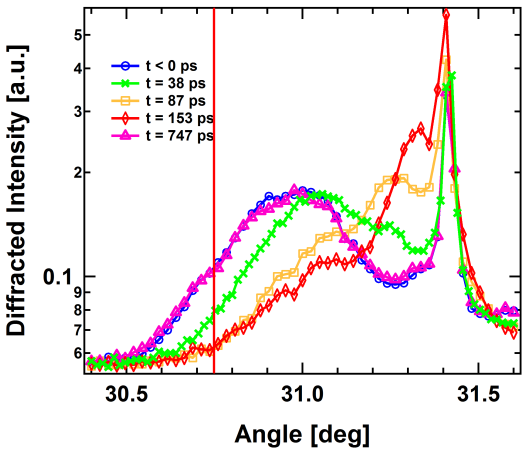

Figure 4.33: (003) PTO/DSO at 430°C: Series of rocking curves for various time-delays on a logarithmic intensity scale. The peak at high angles $\theta = 31.41°$ is the substrate peak. The PTO reflection shifts towards the substrate peak in $\approx$ 100 ps, then fully recovers within less than 1 ns. The red vertical line at$\vartheta = 30.75$ marks the angle at which the time-scan in Fig. 4.36 was measured.

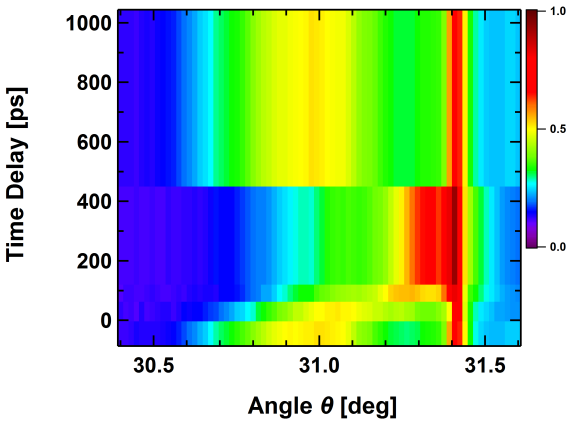

Figure 4.34: False-color image of the rocking curves also shown in Fig. 4.33.

the time-scan. Unfortunately, due to the asymmetric deformation of the rocking curve, the time-scan is to be interpreted with care. For approximately the first 90 ps the drop resembles a shift to higher angles which means a decrease of the c-axis parameter but after 90 ps the peak mainly reshapes and the behavior of the signal of the time-scan cannot be interpreted in terms of a change in the lattice parameter without further ado.

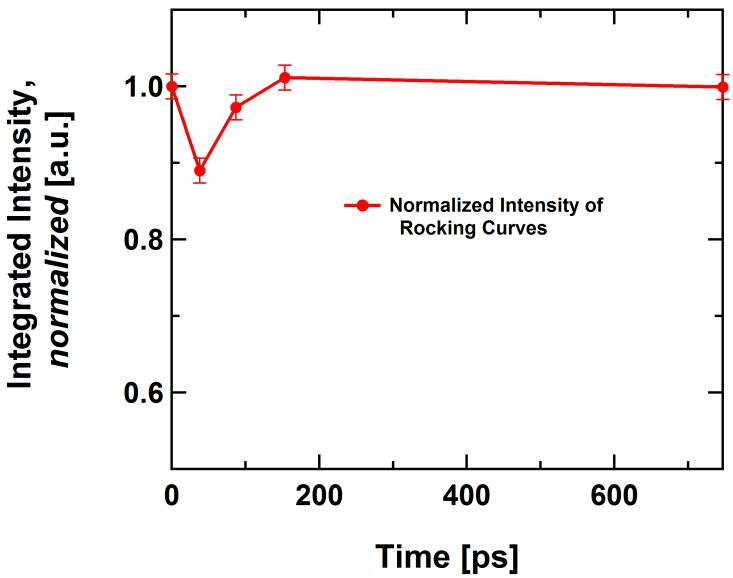

Figure 4.35: Integrated intensity of the rocking curves from Fig. 4.33 as a function of time after laser excitation. The line between the data points is a guide to the eye.

4.3.6 300 nm PTO/DSO Sample, Paralectric Phase

Heating the 300 nm PTO/DSO sample to nominal 450°C causes the tetragonally distorted unit cell of PTO to go in to its paralectric phase with a cubic unit cell.

This can be seen in Fig. 4.37 where the narrow rocking curve, due to the high degree of order in the paralectric phase where the unit cell is cubic or near cubic, exhibits thickness fringes which get washed away by the large width of the rocking curve for the ferroelectric phase. As mentioned at the beginning of this section when discussing the rocking curve at room temperature, this is attributed to the high degree of disorder by the presence of *c*-axis oriented domains and also *a*-axis oriented domains in the ferroelectric phase, but only the *c*-axis domains contribute constructively to the diffraction signal. Table 4.5 shows a comparison of the FWHM of the PTO/DSO rocking curves.

Using the distance of the thickness fringes from the main peak, which originate

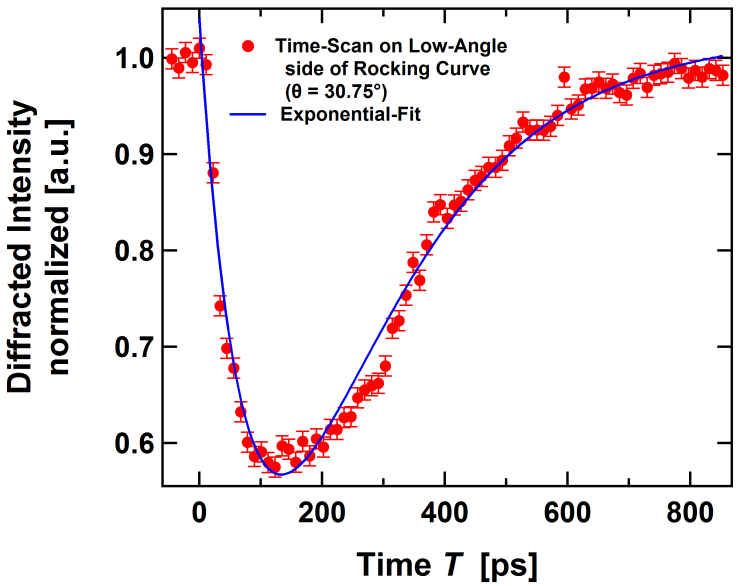

Figure 4.36: Time-scan (red dots) of 300 nm PTO/DSO on the low-angle side of the rocking curve in Fig. 4.33 at $\theta = 30.75°$ fitted with an exponential function (blue line) with time constants $\tau_1 = 91 \pm 13$ ps and $\tau_2 = 200 \pm 32$ ps.

Tabelle 4.5: Difference in width (FWHM) of the rocking curves of the (003) reflection of 300nm PTO on DSO for two temperatures

Sample Temperature [°C]	Time Delay [ps]	FWHM [deg]
Room Temp.	< 0	0,352
450	< 0	0,015

from interferences between the sample surface and the interface to the substrate, we are now able to calculate the thickness of the PTO film. For a sample with the thickness d, the Bragg-angle of the main peak $\theta = 31.31°$ and the X-ray wavelength $\lambda = 0.1378$ nm for a photon energy of 9 keV (see Table 4.3) we can use the following formula [4]

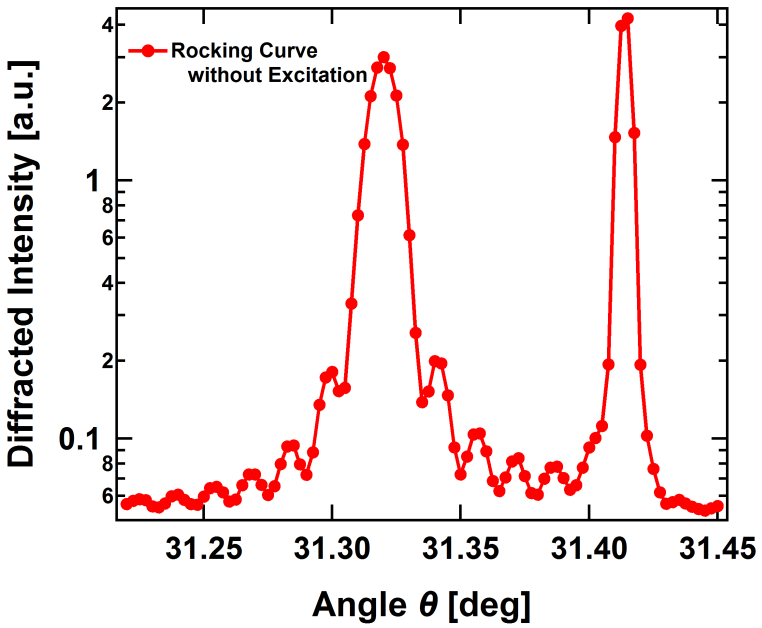

Figure 4.37: 300 nm PTO on (110) DSO at 450°C: Rocking curve in the paralectric phase showing distinct thickness fringes due to the highly ordered crystal at this temperature.

$$d = \frac{\lambda}{2\cos\theta \cdot \Delta\Theta_n} \tag{4.3}$$

by inserting the relative angle between the fringes $\Theta_n = 0.016^\circ$ (average value of all the fringes in Fig. 4.37). This leads to a value for the thickness of

$$d \approx 290nm \tag{4.4}$$

Comparing the lattice parameters for PTO at different temperatures (see Fig. 4.38), calculated from the position of the rocking curves from Eq. 2.2 demonstrate the abrupt change in length of the *c*-axis going from 430°C to 450°C. This again illustrates the temperature dependent length of the *c*-axis of PTO and the behavior at the phase transition temperature, changing from 4.155 Å at room temperature

(Literature value c = 4.1524 Å [62]) to 3.9764 Å at 450°C in the paralectric phase (For comparison: In-plane lattice parameter of DSO at room temperature $a \approx 3.944$ Å [59]).

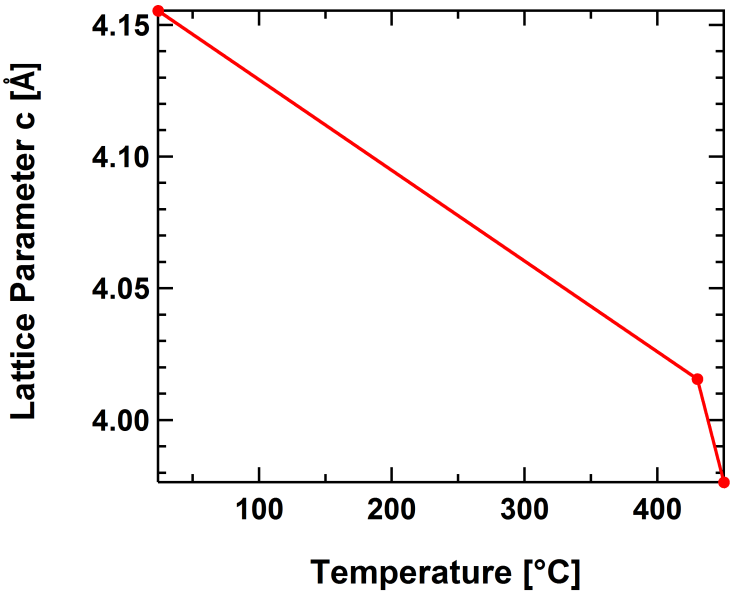

Figure 4.38: C-axis lattice parameter of PTO/DSO plotted against the sample temperature obtained from the position of the (003) Bragg reflection.

Rocking curves for different time-delays after laser excitation with a fluence of 2.7 mJ/cm^2 are shown in Fig. 4.39. After laser excitation a strong asymmetric reshaping/broadening of the curves toward smaller angles combined with a drop in intensity and almost no shift is observed. This indicates an inhomogenic change of the *c*-axis lattice parameter to a larger lattice parameter. Note the significantly smaller angular scale compared to the measurements in Fig. 4.33 and 4.34).

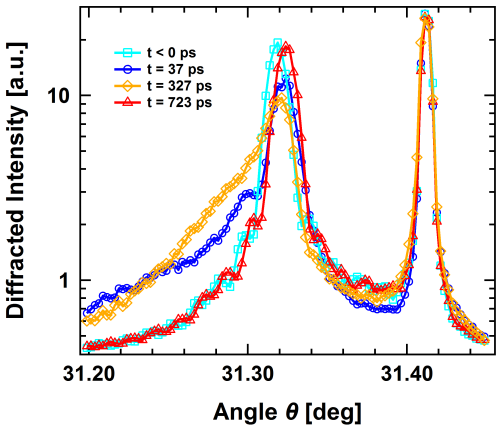

Figure 4.39: 300 nm PTO/DSO at 450°C: Rocking curves for different time-delays after 2.7mJ/cm^2 fluence laser excitation in the paralectric phase. Plotted on a logarithmic intensity scale.

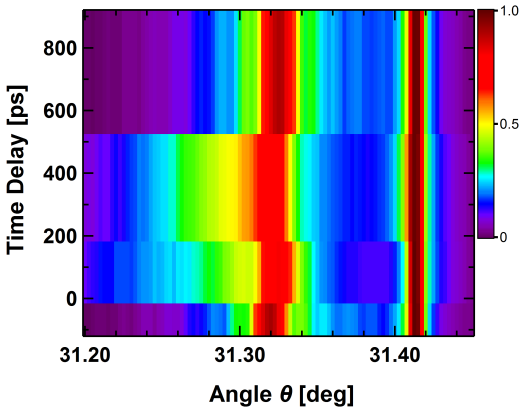

Figure 4.40: False-color image of the rocking curves in Fig. 4.39

4.3.7 Conclusion

20 nm PTO/STO

The measurements carried out at room temperature show that the polarization of the (001) oriented 20 nm PTO thin film grow on (100) STO can be significantly enhanced by laser excitation. This is indicated by observing the transient change of the *c*-axis parameter which is directly coupled to the polarization of the PTO film. In the first 5 ps after excitation a large sound-velocity limited drop of the polarization is observed.

The laser-induced polarization enhancement at higher temperatures (515°C) manifests significantly larger effects. The initial decrease in polarization, however, has nearly disappeared.

The broadened and asymmetrically shaped rocking curve can be attributed to the 180° stripe domain phase [49] forming in thin PZT films.

At both temperatures (room temperature and 515°C) a long lived increase in

polarization is found.

300 nm PTO/DSO

The large width of the rocking curves PTO on DSO are due to the high degree of disorder in the film caused by in- and out-of-plane orientations of the c-axis parameter. This is due to the better lattice match of (001) PTO on (110) Dso (compared to PTO on STO).

Time-resolved measurement at room temperature show very little effect - regarding the reshaping of the rocking curve and the transient shift of the diffraction signal.

At higher temperatures, but below T_C, large effects are observed. By observing the transient reshaping and shift of the rocking curve after laser excitation with 5 mJ/cm^2, we see that the PTO film has almost completely gone in to the cubic paralectric phase, or at least very close. This is indicated by the mergence of the film and the substrate peak while the intensity of the DSO peak increases at the expense of the PTO peak. All this is observed on a time scale of 90 - 150 ps. But the remaining asymmetry of the rocking curve at a delay of 153 ps is an indicator for an incomplete phase transition. After approximately 750 ps the film has completely gone back to its initial state. Further experiments, as planned at UDE, could should be done at a finer time resolution especially to record more data points at time-delays between 87 ps and 700 ps. Here it would also interesting to perform these measurements at higher pump fluences.

To estimate the maximal temperature raise on the surface after exciting the sample with 5mJ/cm2 at 400 nm we use the optical constants $n \approx 3.063$ and $k \approx 0.313$ from the measurements in Fig. **??**. The absorption coefficient is defined as

$$\alpha = \frac{4\pi k}{\lambda}. \tag{4.5}$$

So the deposited energy U an a film with the reflectivity R is

$$U = (1 - R) \cdot F_{in} \cdot \alpha \tag{4.6}$$

where F_{in} is the incident energy fluence from the laser beam. Calculating the reflectivity R for s-polarized light with the *Fresnel*-equation for $\hat{n}_{\text{pto}} = n + \mathrm{i}k = 3.063 + i0.313$ gives R = 0.4975. By knowing the specific heat capacity

$$c_p \cdot \Delta T = U \tag{4.7}$$

we can now calculate ΔT for a given laser fluence F_{in}. By computing the above steps with an absorbtion coefficient $\alpha = 9.83 \cdot 10^4$ cm^{-1} and a reflectivity $R = 0.498$ at an incident angle of 31° from the sample surface we get an absorbed energy of $U \approx 247$ J/cm^3. With a molar heat capacity of $c_p = 150 \frac{\text{J}}{\text{mol} \cdot \text{K}}$ and a density of PTO of 7.9 g/cm^3 [63] we finally get a maximum temperature raise of

$$\Delta T \approx 63^{\circ}\text{K}. \tag{4.8}$$

Comparing the sample temperature of 430°C and the temperature raise of $\Delta T \approx 63$°K from 4.8 we can conclude that the 300 nm film PTO is well heated up to T_C.

At 450°C the PTO film on the DSO substrate is clearly in the near-cubic paraelectric phase. Laser excitation doesn't show the the dramatic shifts towards higher angles,i.e. lower polarization. From this one can conclude that the polarization and thus the c-axis parameter cannot be decreased any further. However we observe the shoulder of the rocking curve going to lower angles. This might be attributed to thermal expansion of the paraelectric lattice. lattice.

Bibliography

[1] Konrad Kopitzki and Peter Herzog. *Einfürung in die Festkörperphysik, 6.Auflage*. Vieweg+Teubner, 2007.

[2] W. H. Zachariasen. *Theory of X-ray Diffraction in Crystals*. Dover Publications, New York, 1994.

[3] M. Sanchez del Rio and R.J. Dejus. XOP: X-ray oriented programs. http://www.esrf.eu/computing/scientific/xop2.1/intro.html; Supported by ESFR and APS.

[4] M. A.G. Halliwell. Practical interpretation of x-ray rocking curves from semiconductor heteroepitaxial layers. *Applied Physics A*, 58, 1994.

[5] C. Thomsen, J. Strait, Z. Vardeny, H. J. Maris, J. Tauc, and J. J. Hauser. Coherent phonon generation and detection by picosecond light pulses. *Phys. Rev. Lett.*, 53, 1984.

[6] C. Thomsen, H. T. Grahn, H. J. Maris, and J. Tauc. Surface generation and detection of phonons by picosecond light pulses. *Phys. Rev. B*, 34, 1986.

[7] Ch. Kittel. *Introduction to Solid State Physics*. Wiley John + Sons, 2004.

[8] M. Ali Omar. *Elementary solid state physics*. Addison-Wesley Publishing Company, 1975.

[9] Tingting Qi, Young-Han Shin, Ka-Lo Yeh, Keith A. Nelson, and Andrew M. Rappe. Collective coherent control: Synchronization of polarization in ferroelectric $pbtio_3$ by shaped thz fields. *Phys. Rev. Lett.*, 102, 2009.

[10] Deutsches Elektronen Synchrotron, Hamburg. http://www.desy.de.

[11] J.N. Galayda representing the LCLS Collaboration at IPAC'10, Kyoto, Japan. *The First Angstrom X-Ray Free-Electron Laser*, 2010.

[12] John N. Galayda, John Arthur, Daniel F. Ratner, and William E. White. X-ray free-electron lasers—present and future capabilities. *J. Opt. Soc. Am. B*, 27(11), 2010.

[13] J.N. Galayda representing the LCLS Collaboration at 8th International Conference on X-ray Lasers, Aspen, Co, USA. *The Linac Coherent Light Source*, 2002.

[14] G. Materlik and Th. Tschentscher, editors. *TESLA Technical Design Report, Part V: The X-Ray Free Electron Laser*. European XFEL GmbH, http://lcdev.kek.jp/TESLA-TDR/, March 2001.

[15] http://lcls.slac.stanford.edu/.

[16] Suresh Narayanan, Alec Sandy, Deming Shu, Michael Sprung, Curt Preissner, and Joseph Sullivan. Design and performance of an ultra-high-vacuum-compatible artificial channel-cut monochromator. *Journal of Synchrotron Radiation*, 15(1):12–18, Jan 2008.

[17] http://www.xfel.eu/de.

[18] http://www-xfel.spring8.or.jp/.

[19] http://www.maxlab.lu.se/.

[20] A. Rousse, P. Audebert, J. P. Geindre, F. Falliès, J. C. Gauthier, A. Mysyrowicz, G. Grillon, and A. Antonetti. Efficient $k\alpha$ x-ray source from femtosecond laser-produced plasmas. *Phys. Rev. E*, 50, Sep 1994.

[21] D. Kühlke, U. Herpers, and D. von der Linde. Soft x-ray emission from subpicosecond laser-produced plasmas. *Applied Physics Letters*, 50(25):1785–1787, 1987.

[22] Margaret M. Murnane, Henry C. Kapteyn, Mordecai D. Rosen, and Roger W. Falcone. Ultrafast x-ray pulses from laser-produced plasmas. *Science*, 251, 1991.

[23] Ch. Reich, P. Gibbon, I. Uschmann, and E. Förster. Yield optimization and time structure of femtosecond laser plasma $k\alpha$ sources. *Phys. Rev. Lett.*, 84, May 2000.

[24] W. Lu, M. Nicoul, U. Shymanovich, A. Tarasevitch, P. Zhou, K. Sokolowski-Tinten, D. von der Linde, M. Mašek, P. Gibbon, and U. Teubner. Optimized k-alpha x-ray flashes from femtosecond-laser-irradiated foils. *Phys. Rev. E*, 80(2), Aug 2009.

[25] M. M. Murnane, H. C. Kapteyn, and R. W. Falcone. High-density plasmas produced by ultrafast laser pulses. *Phys. Rev. Lett.*, 62, Jan 1989.

[26] D. G. Stearns, O. L. Landen, E. M. Campbell, and J. H. Scofield. Generation of ultrashort x-ray pulses. *Phys. Rev. A*, 37, Mar 1988.

[27] U. Shymanovich. *Direct observation of ultrafast atomic motion using time-resolved X-ray diffraction.* Dissertation, Universität Duisburg-Essen, 2007.

[28] B. L. Henke, E. M. Gullikson, and J. C. Davis. X-ray interactions: photoabsorption, scattering, transmission, and reflection at e=50-30000 ev, z=1-92. *Atomic Data and Nuclear Data Tables*, 54(2):181–342, Jul 1993. Web-Interface:

http://henke.lbl.gov/optical-constants/; Supported by Lawrence Berkeley National Laboratory.

[29] M. Nicoul, V. Shymanovich, S. Kähle, T. Caughey, D. Sampat, K. Sokolowski-Tinten, and D. von der Linde. Bent crystal x-ray mirrors for time-resolved experiments with femtosecond laser-produced x-ray pulses. *Journal of Physics: Conference Series*, 21, 2005.

[30] M. Nicoul. *Time-resolved X-ray diffraction with accelerator- and laser-plasma-based X-ray sources*. Dissertation, Universität Duisburg-Essen, 2010.

[31] T. Missalla, I. Uschmann, E. Förster, G. Jenke, and D. von der Linde. Monochromatic focusing of subpicosecond x-ray pulses in the kev range. *Review of Scientific Instruments*, 70, 1999.

[32] U. Shymanovich, F. Quirin, M. Vattilana, W. Lu, M. Nicoul, A.-E. El-Kamhawy, A. Tarasevitch, D. von der Linde, and K. Sokolowski-Tinten. Ultrafast lattice dynamics in ferh during a laser-induced magnetic phase transition. In M. Chergui, D. Jonas, E. Riedle, R. Schoenlein, and A. Taylor, editors, *Ultrafast Phenomena XVII*. Oxford University Press, 2011.

[33] F. Quirin. Zeitaufgelöste röntgenbeugung mit femtosekunden-röntgenpulsen. Diploma thesis, Universität Duisburg-Essen, AG Prof. Bovensiepen, May 2011.

[34] http://www.rcubedsw.com/.

[35] SNLO nonlinear optics code available from A. V. Smith, AS-Photonics, Albuquerque, NM, USA. Website: http://www.as-photonics.com/SNLO.html.

[36] N. A. Pertsev, A. G. Zembilgotov, and A. K. Tagantsev. Effect of mechanical boundary conditions on phase diagrams of epitaxial ferroelectric thin films. *Phys. Rev. Lett.*, 80, 1998.

[37] S. Gariglio, N. Stucki, J.-M. Triscone, and G. Triscone. Strain relaxation and critical temperature in epitaxial ferroelectric $Pb(Zr_{0.2}Ti_{0.8})O_3$ thin films. *Appl. Phys. Lett.*, 90, 2007.

[38] tectra Physikalische Instrumente. Website: http://www.tectra.de/heater.htm.

[39] Heat Wave Labs. Website: http://www.cathode.com/.

[40] FINAL advanced materials. Website: http://www.final-materials.com/de/index.php.

[41] James F. Scott and Carlos A. Paz de Araujo. Ferroelectric memories. *Science*, 246(4936):1400–1405, 1989.

[42] C. H. Ahn, K. M. Rabe, and J.-M. Triscone. Ferroelectricity at the nanoscale: Local polarization in oxide thin films and heterostructures. *Science*, 303(5657):488–491, 2004.

[43] K. J. Choi, M. Biegalski, Y. L. Li, A. Sharan, J. Schubert, R. Uecker, P. Reiche, Y. B. Chen, X. Q. Pan, V. Gopalan, L.-Q. Chen, D. G. Schlom, and C. B. Eom. Enhancement of ferroelectricity in strained batio3 thin films. *Science*, 306, 2004.

[44] H.N. Lee, H.M. Christen, M.F. Chisholm, C.M. Rouleau, and D.H. Lowndes. Strong polarization enhancement in asymmetric three-component ferroelectric superlattices. *Nature*, 433, 2005.

[45] P. Paruch and J.-M. Triscone. High-temperature ferroelectric domain stability in epitaxial $Pb(Zr_{0.2}Ti_{0.8})O_3$ thin films. *Applied Physics Letters*, 88, 2006.

[46] PHASIS, Switzerland, www.PHASIS.ch.

[47] J. Karczewski, B. Riegel, M. Gazda, P. Jasinski, and B. Kusz. Electrical and structural properties of nb-doped $srtio_3$ ceramics. *Journal of Electroceramics*, 24:326–330, 2010.

[48] B. Jaffe, W. J. Cook, and J. Jaffe. *Piezoelectric Ceramics*. Academic Press, London, 1971.

[49] S. K. Streiffer, J. A. Eastman, D. D. Fong, Carol Thompson, A. Munkholm, M. V. Ramana Murty, O. Auciello, G. R. Bai, and G. B. Stephenson. Observation of nanoscale 180° stripe domains in ferroelectric $pbtio_3$ thin films. *Phys. Rev. Lett.*, 89, 2002.

[50] Johannes Frantti, Jyrki Lappalainen, Sten Eriksson, Vilho Lantto, Shigeru Nishio, Masato Kakihana, Sergey Ivanov, and Håkan Rundlöf. Neutron diffraction studies of $pb(zr_xti_{1-x})o_3$ ceramics. *Japanese Journal of Applied Physics*, 39, 2000.

[51] D. D. Fong, A. M. Kolpak, J. A. Eastman, S. K. Streiffer, P. H. Fuoss, G. B. Stephenson, Carol Thompson, D. M. Kim, K. J. Choi, C. B. Eom, I. Grinberg, and A. M. Rappe. Stabilization of monodomain polarization in ultrathin $pbtio_3$ films. *Phys. Rev. Lett.*, 96, 2006.

[52] S. Stephanov. Sergey stephanov's x-ray server. http://sergey.gmca.aps.anl.gov/; Supported by APS.

[53] P.-E. Janolin, B Fraisse, F. Le Marrec, and B. Dkhil. Partial decoupling between strain and polarization on mono-oriented $Pb(Zr_{0.2}Ti_{0.8})O_3$ thin film. *arXiv:0705.3354v1*, 2007.

[54] Dominique de Ligny and Pascal Richet. High-temperature heat capacity and thermal expansion of $SrTiO_3$ and $SrZrO_3$ perovskites. *Phys. Rev. B*, 53(6):3013–3022, Feb 1996.

[55] S. Prosandeev and L. Bellaiche. Asymmetric screening of the depolarizing field in a ferroelectric thin film. *Phys. Rev. B*, 75, 2007.

[56] C. v. Korff Schmising, M. Bargheer, M. Kiel, N. Zhavoronkov, M. Woerner, T. Elsaesser, I. Vrejoiu, D. Hesse, and M. Alexe. Coupled ultrafast lattice

and polarization dynamics in ferroelectric nanolayers. *Phys. Rev. Lett.*, 98(25), 2007.

[57] D. Daranciang, A.M. Lindenberg, and *et al.* Polarization dependent reflectivities were measured as a function of wavelength and incidence angle, then fit to n and k using regression analysis. Contact: daranciang@stanford.edu, aaronl@stanford.edu.

[58] M. V. Ramana Murty, S. K. Streiffer, G. B. Stephenson, J. A. Eastman, G.-R. Bai, A. Munkholm, O. Auciello, and C. Thompson. In situ x-ray scattering study of pbtio[sub 3] chemical-vapor deposition. *Applied Physics Letters*, 80, 2002.

[59] Zhai Z.Y., X.S. Wu, H.L. Cai, X.L. Lu, J.H. Hao, J. Gao, W.S. Tan, Q.J. Jia, H.H. Wang, and Y.Z. Wang. Dislocation density and strain distribution in srtio$_3$ film grown on (1 1 0) dysco$_3$ substrate. *J. Phys. D.: Appl. Phys.*, 42, 2009.

[60] M. Kahn. Acoustic and elastic properties of pzt ceramics with anisotropic pores. *J. Am. Ceram. Soc.*, 68, 1985.

[61] Toshito Mitsui and Jiro Furuichi. Domain structure of rochelle salt and kh_2po_4. *Phys. Rev.*, 90, 1953.

[62] O. Madelung, U. Roessler, and M. Schulz, editors. *Landolt-Börnstein: $SrTiO_3$ and $PbTiO_3$ crystal structure, lattice parameters and density*, volume III/17H-17I-41E. Springer Verlag, 1964.

[63] O. Madelung, U. Roessler, and M. Schulz, editors. *Landolt-Börnstein: Simple perovskite-type oxides - Titanates*, volume III/36A1. Springer Verlag, 1964.